Climate Services 44 (2026) 100706

Contents lists available at ScienceDirect

Climate Services

journal homepage: www.elsevier.com/locate/cliser

Compound patterns and environmental drivers of typhoon disaster chains in southeast coastal China: a multiscale framework

Xiaoliu Yang[a], Laiyin Zhu[b], Xiaochen Qin[c], Xiang Zhou[d], Miaomiao Ma[e], Jiewen You[a,f,g], Ying Chen[a,f,g], Jianhui Wei[h], Lu Gao[a,f,g,*], Harald Kunstmann[h,i,j]

[a] School of Geographical Sciences, Fujian Normal University, Fuzhou 350117, China
[b] School of Environment, Geography, and Sustainability, Western Michigan University, Kalamazoo, MI 49008, USA
[c] Faculty of Geographical Science, Beijing Normal University, Beijing 100875, China
[d] Disaster Reduction Center of Fujian Province, Fuzhou 350001, China
[e] China Institute of Water Resources and Hydropower Research, Beijing 100038, China
[f] Key Laboratory for Humid Subtropical Eco-Geographical Processes of the Ministry of Education, Fujian Normal University, Fuzhou 350117, China
[g] Fujian Provincial Engineering Research Center for Monitoring and Assessing Terrestrial Disasters, Fujian Normal University, Fuzhou 350117, China
[h] Institute of Meteorology and Climate Research (IMKIFU), Karlsruhe Institute of Technology, Campus Alpin, Garmisch-Partenkirchen 82467, Germany
[i] Institute of Geography, University of Augsburg, Augsburg 86159, Germany
[j] Centre for Climate Resilience, University of Augsburg, Augsburg 86159, Germany

A R T I C L E I N F O

Keywords:
Typhoon disaster chain
Compound disaster chain
Disaster-forming environment sensitivity
Vine Copula
XGBoost–SHAP

A B S T R A C T

Typhoons frequently trigger interacting hazards, including river flooding, urban waterlogging, landslides, and storm surge, but disaster records compiled at the event or administrative-unit level limit systematic analysis of their spatial co-occurrence and environmental differentiation. Here, we developed a multiscale framework to quantify chain-specific disaster-forming-environment (DFE) sensitivity for four predefined typhoon disaster chains: typhoon–rainstorm–urban waterlogging (TRU), typhoon–rainstorm–flooding (TRF), typhoon–rainstorm–landslide (TRL), and typhoon–wind–storm surge (TWS). The results revealed a dual spatial pattern, with widespread landslide-related sensitivity in the mountainous interior and localized flood-, waterlogging-, and storm-surge-related sensitivity in coastal areas. TRL had the largest high-sensitivity area, covering 31.6% of Fujian Province, whereas TRU had the smallest spatial extent but was strongly concentrated in coastal urban districts. TRF and TRU exhibited the strongest positive spatial dependence in urban areas (Kendall's τ = 0.834). Areas highly sensitive to at least one chain covered 42.0% of the province and comprised two broad patterns and nine specific types. Single-chain and compound types accounted for 93.1% and 6.9% of this area, respectively, and TRF + TWS was the most extensive compound type, representing 69.4% of the compound-type area. The spatial organization of these types was scale dependent: TRL became increasingly predominant from county to basin scales, indicating that broader-scale aggregation can obscure localized compound-type heterogeneity. Green-space proportion was the leading environmental discriminator for most flood- and coastal-related types, whereas elevation most strongly differentiated TRL. Types containing a TRU component were generally associated with greater impervious-surface coverage and less green space. These findings reveal contrasting inland and coastal patterns of typhoon disaster-chain sensitivity and provide a basis for multiscale hotspot identification and type-specific disaster-chain management.

Practical implications

This study provides a practical framework for identifying priority areas and supporting type-specific management of typhoon disaster chains in regions where chain-specific historical records are limited. By integrating disaster-forming environment (DFE) sensitivity assessment, Vine Copula dependence modelling, multiscale type analysis, and XGBoost–SHAP interpretation, the framework links spatial sensitivity, inter-chain dependence, and environmental differentiation. Three practical implications can be drawn.

* Corresponding author at: School of Geographical Sciences, Fujian Normal University, Fuzhou 350117, China.
E-mail address: l.gao@foxmail.com (L. Gao).

https://doi.org/10.1016/j.cliser.2026.100706
Received 8 November 2025; Received in revised form 18 August 2026; Accepted 19 August 2026
Available online 29 August 2026

First, the results support hotspot-based zoning and differentiated intervention. Highly urbanized coastal districts, such as Taijiang and Huli, should be prioritized for managing flood- and urban-waterlogging-related sensitivity, while low-lying coastal and estuarine areas require additional attention to river flood–storm surge combinations. In areas with high impervious-surface coverage and limited green space, urban planning should limit further surface sealing, improve drainage capacity, and expand blue–green infrastructure, including permeable surfaces, rain gardens, urban green spaces, and retention areas (Venkataramanan et al., 2019; Yang et al., 2026). In inland mountainous areas, management should focus on landslide-related chains through slope monitoring, vegetation restoration, drainage improvement, and local reinforcement where necessary (Yang et al., 2024; Lin et al., 2024).

Second, the findings highlight the need for integrated management of compound disaster chains. The strong dependence between TRF and TRU, together with the absence of a TRU-only type, indicates that high urban-waterlogging sensitivity generally coincides spatially with high river-flood sensitivity. Moreover, TRF + TWS was the most spatially extensive compound type, emphasizing the need for coordinated watershed, estuarine, and coastal management. Emergency management, water resources, natural resources, urban planning, and infrastructure agencies should therefore develop joint response plans for river flooding, urban waterlogging, and storm surge rather than managing these processes independently (Yang et al., 2025; Zamanian et al., 2025).

Third, the framework can inform the design of spatially differentiated multi-hazard early-warning systems. DFE sensitivity maps can guide the spatial prioritization of monitoring and warning resources. In coastal urban areas characterized by strong dependence between TRF and TRU or by the TRF + TWS compound-sensitivity type, warning systems should jointly monitor short-duration rainfall, river discharge or water level, urban drainage and waterlogging conditions, and coastal water levels. In TRL-dominated mountainous areas, greater attention should be given to rainfall, antecedent soil moisture, slope deformation, and locally calibrated landslide indicators. Operational warning thresholds should be calibrated using historical events, local observations, and real-time monitoring data. The SHAP-derived differentiation points identified here can support spatial screening but should not be used as direct operational warning triggers.

1. Introduction

Typhoon disaster chains are common in coastal regions and involve multiple interacting hazard processes. Typhoons generate strong winds, heavy rainfall, and storm surges, which may further lead to river flooding, urban waterlogging, landslides, and coastal inundation. These interconnected processes can occur sequentially or overlap spatially, amplifying regional impacts through cascading interactions (Wang et al., 2024; Xi et al., 2023; Bhardwaj et al., 2020). Under climate change and rapid urbanization, typhoon disaster chains are projected to become more compound and spatially heterogeneous, with increasing uncertainty in their occurrence and impacts (Intergovernmental Panel on Climate Change, 2023; Tang et al., 2023). In southeastern coastal China, mountains and hills, river valleys and plains, and low-lying coastal zones occur in close proximity, while frequent typhoon activity and heterogeneous land-surface conditions favour cascading and compound hazard processes (Yang et al., 2026). Systematically characterizing the spatial sensitivity, inter-chain dependence, and compound patterns of typhoon disaster chains is therefore important for identifying priority areas and supporting differentiated disaster risk reduction.

Disaster-chain identification underpins research on compound hazards. Early studies of disaster chains and cascading hazards relied largely on historical events, field surveys, documentary evidence, and expert judgement, using empirical synthesis and conceptual models to infer triggering relationships and interactions among hazards (Gill and Malamud, 2014; Kappes et al., 2012; Zuccaro et al., 2018). Advances in remote sensing, geographic information systems, reanalysis datasets, and numerical modelling have shifted the field from qualitative description towards spatially explicit quantitative analysis (Wu et al., 2021; Zhou et al., 2025). These approaches enable more systematic characterization of the spatial extent, intensity, and temporal co-occurrence of interacting hazard processes (Zhuang et al., 2023; Cai et al., 2024). In studies of typhoon-related compound events, particular attention has been given to interactions among rainfall, runoff, river flooding, and storm surge. Previous work has coupled river-discharge and storm-surge scenarios to quantify compound-flood frequency and intensity (Deb et al., 2023; Gori et al., 2020), while other studies have combined observations with hydrodynamic models to resolve the spatiotemporal dynamics of rainfall–runoff and coastal-water processes (Dullaart et al., 2021; Moreira et al., 2021). More recently, Copula models and machine-learning approaches have been used to characterize multivariate dependence, joint behaviour, and nonlinear environmental associations, expanding the analytical toolkit for examining compound patterns in typhoon disaster chains (Bodoque et al., 2023; Qin et al., 2025).

However, disaster-chain identification still relies heavily on historical disaster records to determine where particular chains have occurred and how their component hazard processes interact. Although such records provide direct evidence, inconsistent reporting standards, restricted data access, and incomplete spatial coverage often constrain fine-scale and spatially continuous assessment. As a result, poorly documented areas may remain overlooked even where environmental conditions are conducive to the formation of particular disaster chains. The disaster-forming environment (DFE) offers a complementary spatial perspective because underlying environmental conditions shape the formation, development, and spatial differentiation of hazard processes (Dolojan et al., 2025; Ma et al., 2025). Accordingly, DFE sensitivity describes the relative degree to which local environmental conditions favour the potential formation of a given typhoon disaster-chain type. It represents spatial formation potential rather than observed event frequency or temporal occurrence probability (Shi et al., 2020; Wang et al., 2016). Historical evidence can therefore support the identification of representative regional disaster-chain types, whereas DFE sensitivity analysis extends their spatial assessment to areas where fine-scale event records are sparse or unavailable.

Despite recent advances in typhoon disaster-chain and compound-hazard research, three important gaps remain. First, existing studies have largely focused on individual hazards or interactions between pairs of hazard processes, whereas integrated spatial assessments encompassing multiple representative typhoon disaster chains involving river flooding, urban waterlogging, landslides, and coastal inundation remain limited (Chen et al., 2024; Sohrabi et al., 2023; Li et al., 2023). This limitation is particularly evident in regions where disaster records are incomplete or reporting standards are inconsistent. Second, Copula and machine-learning approaches have advanced the analysis of multivariate dependence in compound hazards (Qin et al., 2025; Yang et al., 2026). However, their application to multiple chain-specific sensitivity fields remains limited, particularly in resolving inter-chain dependence, predominant compound types, and their scale-dependent organization. Third, the environmental variables and nonlinear associations that distinguish single- and compound-chain types, including their model-derived differentiation points, remain poorly understood (Sakahira and Hiroi, 2021; Hosseini and Ivanov, 2020). Together, these gaps constrain the development of typhoon disaster-chain research from basic spatial assessment towards interpretable environmental differentiation and more targeted risk management.

To address these gaps, we focus on Fujian Province, China, and examine four representative typhoon disaster chains: typhoon-rainstorm-urban waterlogging (TRU), typhoon-rainstorm-flooding (TRF), typhoon-rainstorm-landslide (TRL), and typhoon-wind-storm surge (TWS). Specifically, we aim to (1) map chain-specific disaster-forming environment (DFE) sensitivity; (2) quantify inter-chain dependence, delineate empirical single- and compound-chain types, and evaluate the scale-dependent organization of these types and their correspondence with model-supported types; and (3) identify the environmental variables and nonlinear associations that differentiate these types. We pursue these objectives using multiple reanalysis and geospatial datasets within an integrated framework combining DFE sensitivity assessment, Vine Copula modelling, multiscale type analysis, and XGBoost-SHAP. The framework provides a basis for sensitivity mapping, priority-area identification, and coordinated multi-hazard management in regions with limited chain-specific historical records.

2. Methods and data

2.1. Study area

Fujian Province (23°33′-28°20′ N, 115°50′-120°40′ E) lies along the southeastern coast of China and has a shoreline length of approximately 3324 km (Yang et al., 2026). The study domain was discretized into 159,532 grid cells at a spatial resolution of 30 arc *sec*. It includes eight primary basins, including the Minjiang Basin, the inland single-inflow combined basin (LS), and the coastal single-inflow combined basin (CS). Administratively, Fujian comprises nine prefecture-level cities and 84 county-level administrative units. For the county-scale analysis, the Pingtan Comprehensive Experimental Zone, whose geographic extent corresponds to Pingtan County, was treated as one county-level administrative unit. Its predominantly mountainous and hilly terrain creates complex hydrogeomorphic conditions that favour the formation of diverse single and compound typhoon disaster chains. Together with the frequent influence of typhoons, these conditions make Fujian a representative region for investigating typhoon disaster-chain sensitivity and compound patterns (Yang et al., 2025).

2.2. Data sources and processing

We compiled multi-source geospatial datasets, including land-use/land-cover data for 2020 (LULC), a digital elevation model (DEM), river and road networks, and other ancillary datasets (Table 1). Terrain variables were derived from the 30-m DEM using ArcGIS 10.7. Slope and profile curvature (PC) were calculated using the Slope and Curvature tools, respectively. The topographic wetness index (TWI), stream power index (SPI), and sediment transport index (STI) were derived from slope and upslope contributing area following established formulations (Moore et al., 1991). Relief intensity (RI) was calculated as the difference between the maximum and minimum elevations within a 3 × 3-cell moving window. The terrain ruggedness index (TRI) was calculated within the same neighbourhood as the square root of the summed squared elevation differences between the central cell and its eight adjacent cells (Riley et al., 1999). (See Fig. 1.)

LULC data were processed separately to derive green-space proportion (PGS), impervious-surface proportion (ISP), and land-cover type reclassification (LTR). For PGS, cropland, forest, and grassland were grouped as green space. For ISP, urban land, rural settlements, and other built-up land were grouped as impervious surfaces. PGS and ISP were calculated as the areal proportions of the corresponding 30-m LULC classes within each 30-arc-second analysis grid cell. For the TWS sensitivity assessment, LULC was separately reclassified as the ordinal LTR variable. Impervious surfaces, cropland, wetlands, vegetation, and other land-cover types were assigned scores of 10, 8, 6, 4, and 2, respectively, with higher scores indicating greater DFE sensitivity. Cropland was retained as a separate class, whereas forest and grassland were grouped as vegetation.

All variables were harmonized to a spatial resolution of 30 arc *sec* using procedures appropriate to their data types. These datasets were used to construct the chain-specific DFE sensitivity indices and as environmental predictors in the XGBoost–SHAP analysis, whereas the resulting continuous DFE sensitivity indices were used in the Vine Copula models.

2.3. Research framework

The following subsections provide detailed descriptions of the methods corresponding to the three analytical stages presented in Fig. 2.

2.3.1. Definition and DFE sensitivity assessment of representative typhoon disaster chains

The four representative chains examined in this study—TRU, TRF, TRL, and TWS—were identified in our previous regional studies based on disaster reports for 29 typhoons that affected Fujian Province during 2009–2020, together with process-based understanding and supporting literature (Yang et al., 2024, 2025). These reports provided the empirical basis for the regional chain typology but were compiled mainly at the event or administrative-unit scale and therefore did not provide spatially complete grid-level occurrence records. To enable fine-scale spatial assessment, we quantified chain-specific DFE sensitivity at the

Table 1
Data sources and variables used in this study.

Category	Data name	Abbreviation	Unit	Resolution	Data resource
Land use and land cover (LULC 2020)	Green space proportion	PGS	%	30 m	Data Center for Resources and Environmental Sciences (https://www.resdc. cn/)
	Impervious surface proportion	ISP	%	30 m	
	Reclassification of land cover types	LTR	–	30 m	
Road network data (2020)	Distance from roads	DFO	m	–	OpenStreetMap Data https://www.openstreetmap.org
River network data (2020)	Distance from rivers	DFR	m	–	
	Drainage density	DD	km/km^2	–	
Normalized Difference Vegetation Index	Normalized difference vegetation index	NDVI	–	30 m	Data Center for Resources and Environmental Sciences (https://www.resdc. cn/)
Fracture zone data	Distance from fault zones	DFFZ	m	–	
Digital Elevation Model	Elevation	DEM	m	30 m	
	Topographic wetness index	TWI	–	30 m	
	Stream power index	SPI	–	30 m	
	Relief intensity	RI	m	30 m	
	Sand transport index	STI	–	30 m	
	Profile curvature	PC	–	30 m	
	Slope	Slope	°	30 m	
	Terrain roughness index	TRI	–	30 m	
Coastal Data Engine	Distance from the coastline	CFD	m	30 m	China Coastal Dataset https://coastaldata.ecnu.edu.cn/zh-hans/node/125

Note: The "–" symbol in the "Unit" column indicates vector data, which have no spatial resolution.

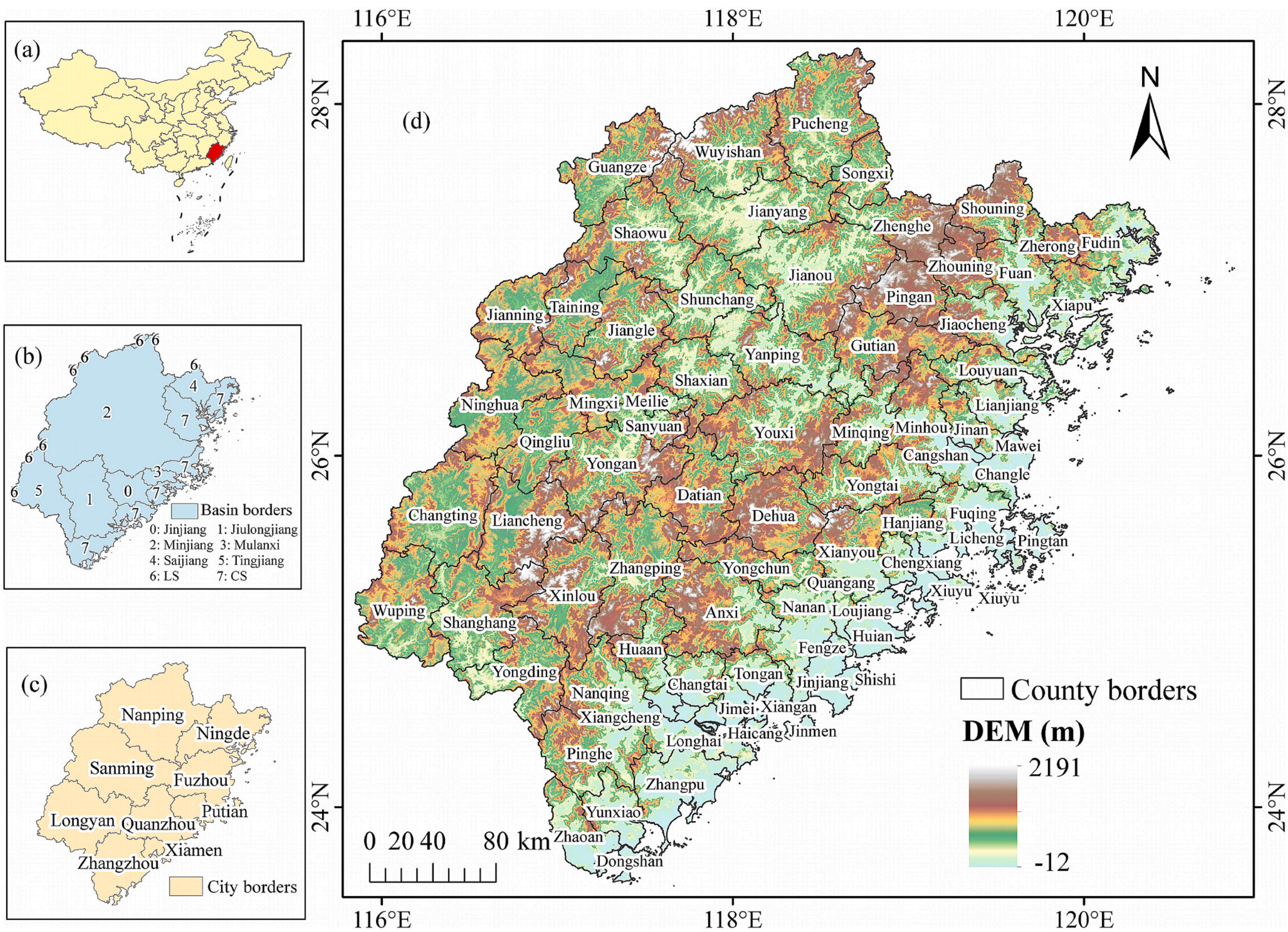

Fig. 1. Overview of the study area: (a) location of Fujian Province within China; (b) river basins; (c) the nine prefecture-level cities; and (d) county-level administrative boundaries and digital elevation model (DEM). The Pingtan Comprehensive Experimental Zone, whose geographic extent corresponds to Pingtan County, was included in the county-level analysis shown in (d).

grid-cell level using environmental indicators. Following the regional disaster-system framework, DFE sensitivity was operationalized as the relative degree to which local environmental conditions favour the potential formation of a given chain, rather than its observed occurrence frequency or temporal probability (Shi et al., 2020).

Based on the formation processes and relevant environmental conditions of each chain, we developed a chain-specific DFE indicator system. The selected indicators represent topographic, hydrological, land-cover, vegetation, geological, anthropogenic, and coastal conditions associated with the formation of the four chains. Table 2 summarizes the indicators included in each chain-specific index, their expected directional relationships with DFE sensitivity, and the supporting references.

The indicator sets differed among the four disaster chains because each chain involves distinct formation processes and environmental conditions. TRU was characterized primarily by local topographic, drainage, and urban land-cover conditions; TRF and TRL were represented by broader combinations of topographic, hydrological, vegetation, and geomorphic indicators; and TWS was characterized mainly by coastal elevation, proximity to the shoreline, slope, and land-cover characteristics. Indicators were therefore selected according to the formation characteristics of each chain rather than by imposing an identical number of indicators across all four chains. The potential uncertainty associated with differences in indicator composition is further considered in the limitations.

The DFE sensitivity assessment comprised six steps: indicator standardization, subjective weighting, objective weighting, combined weighting, continuous-index calculation, and sensitivity classification.

First, all indicators were standardized to make variables with different units and ranges comparable. Positive and negative indicators were normalized as follows:

$$\text{For positive indicators}: Y_{\text{ij}} = \frac{X_{ij} - X_{\min}}{X_{\max} - X_{\min}} \tag{1}$$

$$\text{For negative indicators}: Y_{ij} = \frac{X_{\max} - X_{\text{ij}}}{X_{\max} - X_{\min}} \tag{2}$$

where Y_{ij} is the standardized value of the j-th indicator for the i-th unit; $X_{\max}$ and $X_{\min}$ are the maximum and minimum of the indicator. After standardization, larger values consistently indicated higher DFE sensitivity (Moreira et al., 2021; Dawit et al., 2023).

Second, subjective indicator weights were derived using the Analytic Hierarchy Process (AHP). Five experts specializing in disaster science, hydrology, and meteorology who participated in the Fujian component of China's First National Comprehensive Risk Survey of Natural Disasters conducted pairwise comparisons of the indicators. The relative importance of each indicator pair was evaluated using Saaty's 1–9 scale, where 1 represents equal importance and 9 represents the extreme importance of one indicator over another (Karim et al., 2023). A judgement matrix was constructed for each expert and each chain-specific indicator set. Matrix consistency was evaluated using the consistency ratio (CR); matrices with CR $<$ 0.10 were retained, whereas those failing this criterion were reassessed. The final AHP weight of each indicator was obtained by averaging its normalized weights across all valid expert judgement matrices.

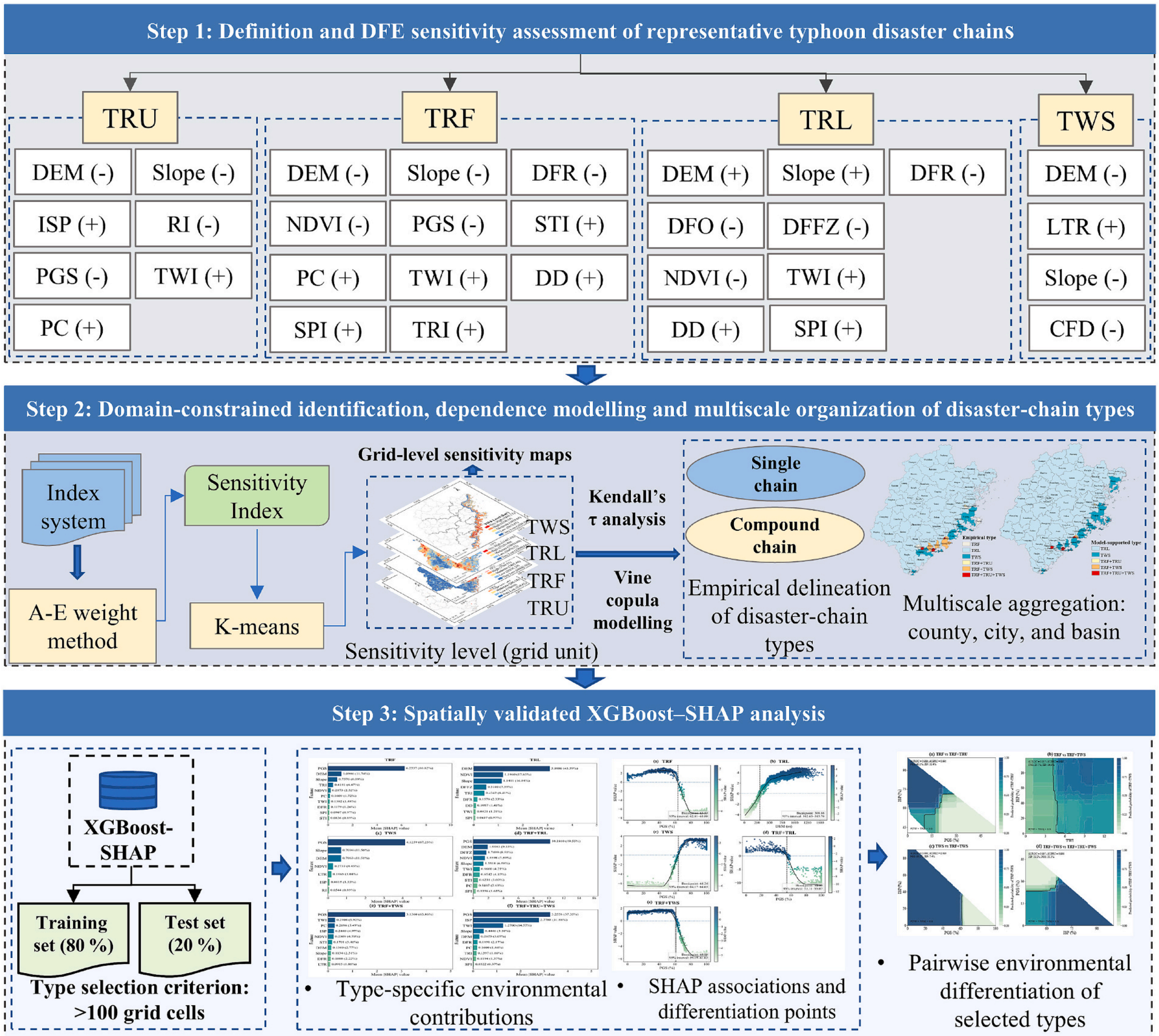

Fig. 2. Overall design and analytical framework of the study. TRU denotes typhoon–rainstorm–urban waterlogging; TRF, typhoon–rainstorm–flooding; TRL, typhoon–rainstorm–landslide; and TWS, typhoon–wind–storm surge.

Table 2
Disaster-forming environment indicators used for the four representative typhoon disaster chains and their expected directional relationships with DFE sensitivity.

Indicator	Abbreviation	TRU	TRF	TRL	TWS	Supporting references
Elevation	DEM	–	–	+	–	Ye et al., 2022; Meng et al., 2023; Bhardwaj et al., 2020
Slope	Slope	–	–	+	–	Ye et al., 2022; Liu et al., 2020
Profile curvature	PC	+	+	/	/	Lin et al., 2022; Li, 2022; Zhang et al., 2021
Topographic wetness index	TWI	+	+	+	/	Schwarz and Kuleshov, 2022; Lee et al., 2017; He et al., 2019
Impervious surface proportion	ISP	+	/	/	/	Bi et al., 2022; Ermagun et al., 2024
Green space proportion	PGS	–	–	/	/	Bi et al., 2022; Ermagun et al., 2024; Zeng et al., 2024
Relief intensity	RI	–	/	/	/	Yang et al., 2025
Normalized difference vegetation index	NDVI	/	–	–	/	Zeng et al., 2024; Ye et al., 2022
Stream power index	SPI	/	+	+	/	Schwarz and Kuleshov, 2022; He et al., 2019
Terrain roughness index	TRI	/	+	/	/	Salman et al., 2023
Sediment transport index	STI	/	+	/	/	Salman et al., 2023; Yu and David, 2022
Drainage density	DD	/	+	+	/	Dou et al., 2020
Distance from rivers	DFR	/	–	/	/	Falguni and Singh, 2020
Distance from fault zones	DFFZ	/	/	–	/	Dou et al., 2020
Distance from roads	DFO	/	/	–	/	Wang et al., 2016
Land-use type reclassification	LTR	/	/	/	+	Liu et al., 2023
Distance from coastline	CFD	/	/	/	–	Liu et al., 2020; Meng et al., 2023

Note: "+" and "–" indicate expected positive and negative relationships with DFE sensitivity, respectively. "/" indicates that the indicator was not included in the corresponding chain-specific index. For LTR, "+" denotes land-cover classes assigned higher DFE sensitivity scores for TWS.

Third, objective weights were calculated separately for each chain using the entropy method. The entropy weight of each indicator was determined from the spatial variation in its standardized values, such that indicators containing greater spatial information received larger weights, whereas spatially uniform indicators received smaller weights. The calculation followed the entropy-weighting procedure described by Yang et al. (2025).

Fourth, the AHP and entropy weights were integrated using the distance-function combination method described by Yang et al. (2025). Let w_j^{AHP} and w_j^{ENT} denote the normalized AHP and entropy weights of indicator j, respectively. The distance between the two weight vectors was calculated as

$$d = \left[\frac{1}{2}\sum_{j=1}^{m}\left(w_j^{AHP} - w_j^{ENT}\right)^2\right]^{1/2} \tag{3}$$

The combination coefficients were determined by solving

$$d^2 = (\alpha - \beta)^2, \alpha + \beta = 1, \quad \alpha > 0, \beta > 0 \tag{4}$$

This procedure yielded $\alpha = 0.4493$ for the AHP component and $\beta = 0.5507$ for the entropy component. The final weight of indicator j for disaster chain k was then calculated as

$$w_{jk} = \alpha w_{jk}^{AHP} + \beta w_{jk}^{ENT} \tag{5}$$

Because the AHP and entropy weight vectors were normalized separately within each chain and $\alpha + \beta = 1$, the resulting combined weights also summed to one within each chain. This ensured that a chain-specific index did not receive a larger total weight solely because it contained more indicators.

Fifth, a continuous DFE sensitivity index was calculated for each disaster chain in every grid cell:

$$S_{ik} = \sum_{j=1}^{m_k} w_{jk} Y_{ij} \tag{6}$$

where S_{ik} is the DFE sensitivity index of chain k in grid cell i, m_k is the number of indicators included in the index for chain k, w_{jk} is the combined weight of indicator j for chain k, and Y_{ij} is the corresponding standardized indicator value.

Finally, K-means clustering was applied separately to the continuous DFE sensitivity index of each chain. A five-cluster solution was retained after jointly considering the elbow criterion and the average silhouette coefficient. The resulting clusters were ordered according to their mean index values and classified as Very Low, Low, Moderate, High, and Very High (Yang et al., 2025; Xiao et al., 2023). The continuous index values were retained for the subsequent dependence and Vine Copula analyses, whereas the discrete classes were used for sensitivity mapping. The High and Very High classes were jointly defined as high-sensitivity areas.

2.3.2. Domain-constrained identification, dependence modelling and multiscale organization of disaster-chain types

The Vine Copula models were fitted to spatially thinned samples of the continuous, chain-specific DFE sensitivity indices derived at the 30-arc-second grid-cell scale within each common applicability domain. The original environmental indicators, discrete K-means classes, and historical disaster-occurrence records were not used as Copula variables. Historical disaster reports were used only to support the prior identification and definition of TRU, TRF, TRL, and TWS.

TRF and TRL were evaluated throughout Fujian Province, whereas TRU was restricted to urban areas and TWS to the 10-km coastal zone. Cells outside the applicability domain of a chain were treated as not applicable rather than assigned zero sensitivity. Accordingly, the study area was divided into four mutually exclusive domains: D00, where neither TRU nor TWS was applicable; D10, where only TRU was applicable; D01, where only TWS was applicable; and D11, where both were applicable. TRF and TRL were applicable in all four domains.

High-sensitivity status was defined independently of the Copula models. For each chain, the lower boundary of the High class in the five-class K-means classification was used as the threshold, and cells classified as High or Very High were designated as high sensitivity. The binary maps of all applicable chains were then directly overlaid. Combinations containing one high-sensitivity chain were classified as single-chain patterns, whereas those containing two or more were classified as compound-chain patterns. For a domain with d applicable chains, at most $2^d - 1$ non-empty combinations were possible after excluding the all-non-high state. These combinations represent the spatial co-location of high DFE sensitivity rather than observed simultaneous disaster occurrence. Compound types are denoted by joining the abbreviations of their component chains with a plus sign (e.g., TRF + TWS).

Pairwise dependence was evaluated within the common applicability domain of each chain pair using rank-based pseudo-observations, Kendall's τ, and LOWESS curves. To reduce local spatial redundancy, one grid cell was retained within each 2-km spatial block, with a 1-km fallback where required. Copula models were fitted separately for D00, D10, D01, and D11. Candidate models included independence, parametric bivariate Copulas, parametric C-vines and R-vines, and flexible R-vines with non-parametric pair-Copulas where sample size permitted. Complete 50-km spatial blocks were allocated to either the training or test set. Model selection was based primarily on test-set mean log-likelihood, with AIC, BIC, Rosenblatt diagnostics, and observed–simulated comparisons used as complementary criteria (Aas et al., 2009; Ganguli and Merz, 2024).

For each selected model, 200,000 fixed-seed quasi-random samples were generated and classified using the chain-specific high-sensitivity thresholds. The resulting probabilities represent the spatial prevalence of mutually exclusive disaster-chain types within each domain, rather than their temporal probability of occurrence. Empirical grid-level classification remained based on the direct overlay.

Grid-level types and domain-specific Copula probabilities were summarized at county, prefecture-level city, and basin scales. Within each geographic unit, the predominant empirical type was defined as the non-empty type occupying the largest area. Spatial type diversity was measured using Shannon entropy:

$$H_g = -\sum\nolimits_{s=1}^{M_g} q_{gs} \ln q_{gs} \tag{7}$$

where q_{gs} is the proportion of the total non-empty type area occupied by type s in geographic unit g, and M_g is the number of non-empty types present. Higher values indicate a more even and diverse type composition (Lin et al., 2024).

Domain-specific Copula probabilities were aggregated using the area proportions of the corresponding domains within each geographic unit. The non-empty type with the largest area-weighted probability was defined as the model-supported type. A mismatch was recorded when the model-supported type differed from the predominant empirical type. Agreement between the complete empirical and model-supported type distributions was measured using total variation distance:

$$TV_g = \frac{1}{2}\sum_s \left| q_{gs} - p_{gs} \right| \tag{8}$$

where q_{gs} and p_{gs} are the empirical and model-supported proportions of type s in geographic unit g, respectively. Smaller TV_g values indicate closer agreement between the two distributions.

2.3.3. Spatially validated XGBoost-SHAP analysis

We used XGBoost and SHapley Additive exPlanations (SHAP) to characterize the environmental associations and nonlinear differentiation of the mapped disaster-chain types. The response labels were the mutually exclusive types identified by the direct spatial overlay. For each target type, a one-versus-rest model was constructed using only non-empty types within its applicability domain. Grid cells outside the applicable domains of TRU and TWS were not treated as negative samples. Predictors included the environmental indicators associated with the component chains of each type (Dey et al., 2024; Peng et al., 2025).

Grid cells were grouped into 50-km spatial blocks to reduce spatial dependence between training and evaluation samples. Complete blocks were assigned to either the training set or an independent 20% test set. Model parameters were selected using stratified spatial group cross-validation within the training data. Class imbalance was addressed by weighting the positive class according to the ratio of negative to positive training samples, while the original class proportions were retained in the test set. Model performance was evaluated using AUROC, AUPRC and balanced accuracy, and only models meeting the predefined sample-size and performance criteria were interpreted using SHAP.

SHAP values were calculated for the independent test samples using TreeExplainer. The global importance of predictor j was quantified as:

$$I_j = \frac{1}{n}\sum_{i=1}^{n}|\phi_{ij}| \tag{9}$$

where ϕ_{ij} is the SHAP value of predictor j grid cell i. Relative contributions were calculated using the summed mean absolute SHAP values of all predictors in the corresponding model. Nonlinear associations were evaluated using LOWESS-smoothed relationships between predictor values and SHAP values. The principal crossing of the smoothed curve through SHAP $=0$ was identified as a model-derived differentiation point, representing a change in the sign of the predictor's contribution to the fitted model. Uncertainty was estimated by spatial block bootstrap resampling, and only relationships with stable 95% intervals were

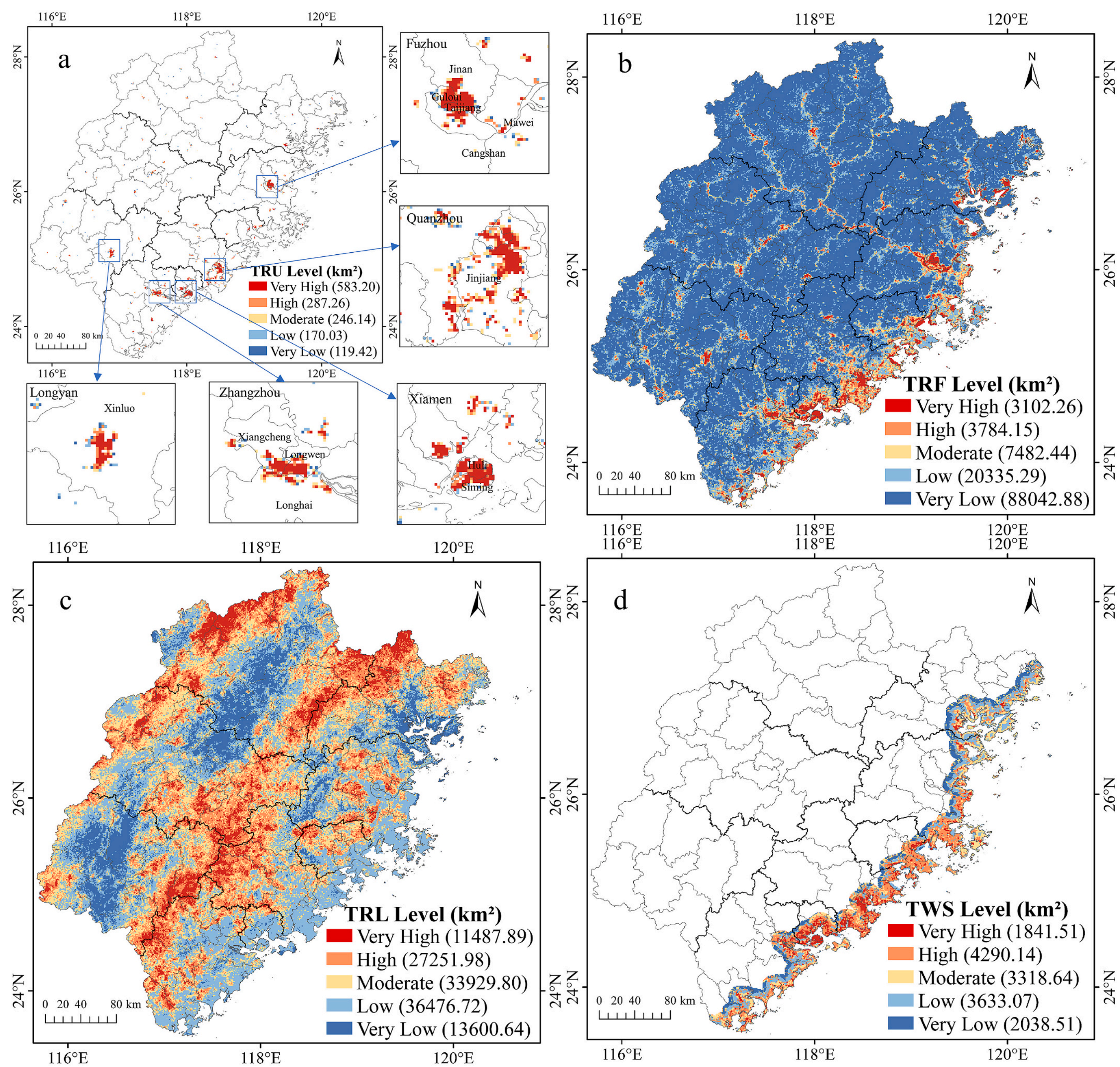

Fig. 3. Spatial patterns of single typhoon disaster-chain sensitivity in Fujian Province. (a) Typhoon–rainstorm–urban waterlogging (TRU); (b) typhoon–rainstorm–flooding (TRF); (c) typhoon–rainstorm–landslide (TRL); and (d) typhoon–wind–storm surge (TWS).

retained.

The second component was pairwise environmental differentiation analysis. For selected comparisons between a single-chain type and a compound-chain type sharing the same applicability domain (e.g., TRF versus TRF + TRU), we constructed a balanced binary dataset using samples from the two spatial classes. The analysis was applied only to type pairs with sufficient sample sizes. Predictors were ranked according to their mean absolute SHAP values.

Pairwise models were further constructed for selected types sharing a common applicability domain. For each comparison, the two predictors with the largest mean absolute SHAP values were varied across their 5th–95th percentile ranges, while the remaining predictors were fixed at their training-set medians:

$$p_t(x_1, x_2) = f(x_1, x_2, m) \tag{10}$$

where p_t is the predicted probability of the target type t, x_1 and x_2 are the two leading predictors, and m represents the median values of all remaining predictors. Response surfaces were restricted to the observed bivariate support, and the $P = 0.5$ contour represented the decision boundary between the two types.

3. Results

3.1. Spatial patterns of single disaster-chain sensitivity

We first examined the disaster-forming-environment sensitivity of four single typhoon disaster chains in Fujian Province. The four chains showed distinct spatial patterns (Fig. 3). TRU was highly localized in coastal built-up areas, whereas TRF extended along river valleys and downstream coastal areas (Fig. 3a, b). TRL was mainly distributed in the mountainous and hilly areas of central and western Fujian, while TWS was restricted to low-lying coastal and estuarine areas (Fig. 3c, d).

The extent of high-sensitivity areas differed markedly among the four chains. TRL had the largest high-sensitivity area, covering 38,739.87 km^2, or 31.6% of the province, indicating that landslide-related typhoon disaster chains were the most widespread in Fujian (Fig. 3c). TRF and TWS covered 6886.41 km^2 and 6131.65 km^2, accounting for 5.6% and 5.0% of the province, respectively (Fig. 3b, d). In contrast, TRU had the smallest high-sensitivity area, covering 870.46 km^2, or 0.7% of the province, but it was strongly clustered in highly urbanized coastal districts (Fig. 3a).

Multiscale results further showed that high-sensitivity areas were concentrated in coastal cities and downstream basins, but the dominant chain type varied with environmental setting. The coastal single-inflow combined basin (CS) contained the largest high-sensitivity areas for TRU, TRF, and TWS, highlighting the role of coastal lowlands and downstream river systems. Quanzhou, Fuzhou, Xiamen, and Zhangzhou were major hotspots for TRU-, TRF-, and TWS-related sensitivity, whereas Nanping and Sanming showed stronger TRL sensitivity because of their mountainous terrain. At the county scale, highly urbanized districts such as Taijiang and Huli showed high TRU and TRF sensitivity. For example, high TRU sensitivity accounted for 91.7% of Taijiang and 87.4% of Huli, indicating strong local concentration in coastal urban districts. Overall, Fujian showed a dual sensitivity pattern. Landslide-related sensitivity was widespread in inland mountains, while TRF-,

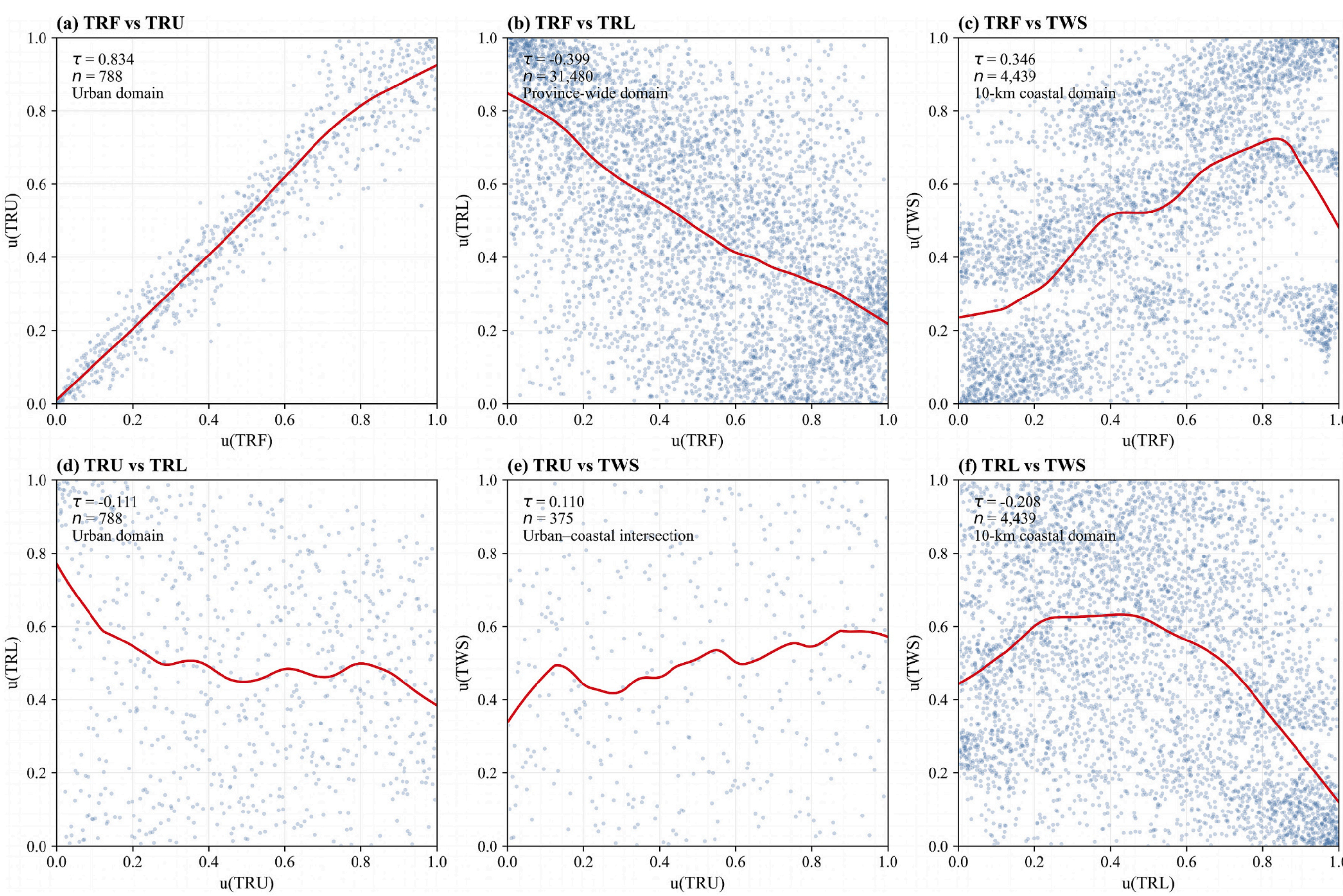

Fig. 4. Pairwise spatial dependence among the continuous DFE sensitivity indices of four typhoon disaster chains in Fujian Province. Blue points denote rank-transformed pseudo-observations from the 2-km spatially thinned samples, and red curves denote LOWESS smoothers. Insets report Kendall's τ, sample size (n), and the common applicability domain for each chain pair. All axes are expressed on the unit interval. The LOWESS curves are descriptive and were not used for model fitting or selection. (For interpretation of the references to colour in this figure legend, the reader is referred to the web version of this article.)

TRU-, and TWS-related sensitivity was concentrated in coastal urban areas.

3.2. Dependence structure and scale-dependent organization of disaster-chain types

Pairwise analysis revealed contrasting spatial dependence patterns among the continuous DFE sensitivity indices (Fig. 4). The strongest positive dependence occurred between TRF and TRU in urban areas ($\tau = 0.834$), where the two indices followed an almost monotonic relationship in rank space. TRF and TWS were also positively associated within the 10-km coastal zone ($\tau = 0.346$), although the association weakened at the highest TRF ranks. In contrast, TRL showed negative spatial associations with TRF across the province ($\tau = -0.399$) and with TWS within the coastal zone ($\tau = -0.208$). The remaining relationships involving TRU were weak ($|\tau| \leq 0.111$). These patterns indicate close spatial alignment between flood and urban-waterlogging sensitivity, moderate alignment between flood and storm-surge sensitivity along the coast, and a contrasting spatial distribution of landslide-related sensitivity. Domain-specific model selection based on 50-km spatial-block hold-out validation favoured different dependence structures across the four applicability domains (Table S1), indicating that no single Copula structure was imposed across the study area.

The spatial overlay delineated 51,561.1 km^2, or 42.0% of Fujian Province, as highly sensitive to at least one disaster chain, comprising two broad patterns and nine specific chain types (Fig. 5). The areal composition was strongly uneven. Single-chain types accounted for 93.1% of the total high-sensitivity area, with the TRL-only type alone representing 80.2%, whereas compound-chain types occupied only 6.9%. Compound sensitivity was nevertheless concentrated in a few dominant combinations: TRF + TWS accounted for 69.4% of the compound-chain area, followed by TRF + TRU + TWS and TRF + TRU. No TRU-only type was identified, indicating that high urban-waterlogging sensitivity occurred in combination with flood-related sensitivity rather than independently. Overall, the provincial pattern was characterized by extensive landslide-related single-chain sensitivity and more localized compound sensitivity associated primarily with flood–coastal and flood–urban combinations. At the broader pattern level, the area-weighted proportions derived from the Copula probabilities were highly consistent with those obtained from the spatial overlay. The proportions of single- and compound-chain patterns were 93.08% and 6.92% based on the Copula estimates, compared with 93.14% and 6.86% based on the spatial overlay, respectively.

Multiscale aggregation showed that the dominance of TRL became more pronounced with increasing spatial scale (Fig. 6). TRL was the predominant empirical type in 71.8% of counties, 88.9% of cities, and all basins, and was also the most frequent model-supported type at each scale. The mismatch between the predominant empirical and model-supported types declined from 12.9% at the county scale to 11.1% at the city scale and disappeared at the basin scale. The median total variation distance between the empirical and modelled type distributions similarly decreased from 0.063 for counties to 0.039 for cities and 0.035 for basins. Empirical type entropy nevertheless remained high in selected spatial units, including the CS and Mulanxi basins, indicating that a common predominant type did not necessarily imply internally uniform type composition. These results indicate a clear scale dependence: county-level aggregation retains more localized compound-chain differentiation, whereas aggregation to city and basin scales increasingly smooths this heterogeneity beneath a widespread TRL-dominated background.

3.3. Environmental associations and nonlinear differentiation of disaster-chain types

Seven of the nine mapped disaster-chain types met the sample-size criteria for XGBoost modelling. Six of these also met the performance criteria for SHAP interpretation, with spatial holdout AUROC values of 0.929–0.999 and balanced accuracies of 0.865–0.984. The TRF + TRU one-versus-rest model showed weaker discrimination than the other type-specific models (AUROC = 0.705; balanced accuracy = 0.591) and was not included in the subsequent SHAP interpretation. Environmental contributions varied substantially among the retained types (Fig. 7). PGS was the leading contributor for TRF, TWS, TRF + TRL, TRF + TWS and TRF + TRU + TWS, accounting for 37.4–67.2% of the total mean absolute SHAP value. In contrast, DEM was the leading contributor for TRL, accounting for 45.6%. Green-space coverage therefore represented the main environmental gradient associated with most flood- and coastal-related types, whereas elevation was more strongly associated with the differentiation of the landslide-related type.

The leading environmental associations were nonlinear (Fig. 8). Stable SHAP zero crossings occurred at PGS values of 63.53% for TRF and 64.24% for TWS. The corresponding values were lower for TRF + TRL and TRF + TWS, at 54.00% and 60.98%, respectively. TRL showed a different response, with its principal SHAP zero crossing occurring at an elevation of 308.86 m. The locations of these zero crossings differed among types, showing that disaster-chain types associated with the same

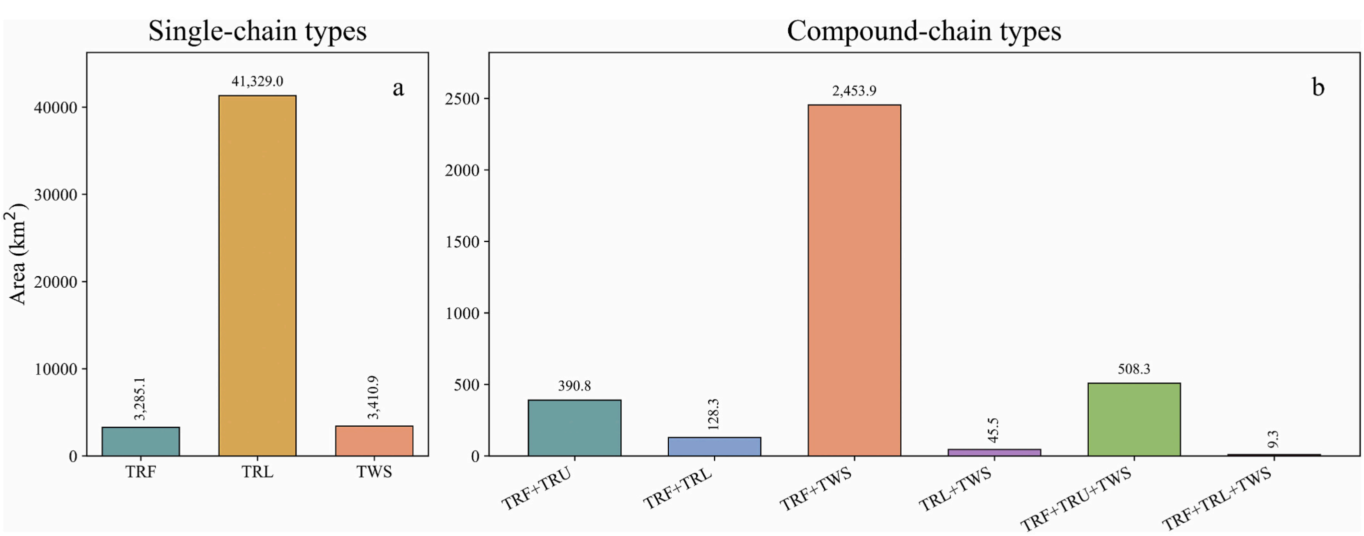

Fig. 5. Areal extent of disaster-chain types within the two identified patterns. (a) Areas of the three single-chain types; (b) areas of the six compound-chain types identified across Fujian Province.

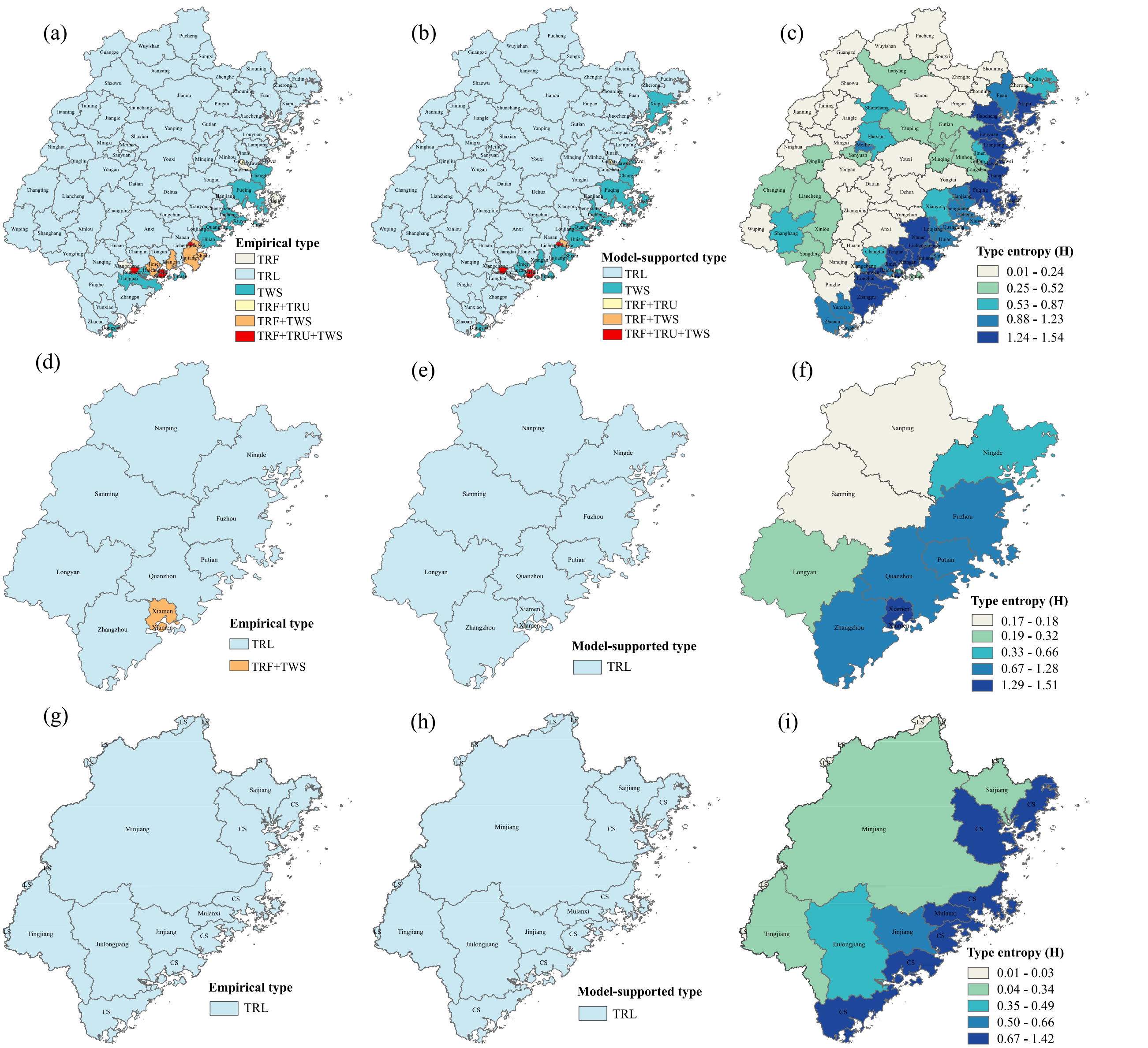

Fig. 6. Multiscale organization of disaster-chain types in Fujian Province. (a, d, g) Predominant empirical types; (b, e, h) model-supported types; and (c, f, i) empirical type entropy (H) at the county (a–c), city (d–f), and basin (g–i) scales. Higher H indicates a more even and diverse type composition.

leading variable nevertheless occupied distinct parts of the environmental gradient.

Pairwise models further resolved environmental differences between selected types (Fig. 9), with AUROC values ranging from 0.857 to 0.999. The separation between TRF and TRF + TRU was dominated by PGS and ISP, which accounted for 40.2% and 32.4% of the total mean absolute SHAP value, respectively. The low-PGS–high-ISP combination produced the highest mean predicted probability of TRF + TRU ($P = 0.996$). The separation between TRF and TRF + TWS was distributed across a broader set of predictors: TWI and ISP contributed 25.7% and 14.0%, respectively, and the high-TWI–high-ISP combination produced the highest mean predicted probability of TRF + TWS ($P = 0.777$).

PGS was the principal variable differentiating TWS from TRF + TWS, contributing 55.2%, compared with 7.4% for ISP. Under low-PGS–high-ISP conditions, the mean predicted probability of TRF + TWS approached 1.000. TRF + TRU + TWS was distinguished from TRF + TWS mainly by ISP and PGS, which contributed 39.2% and 31.3%, respectively. The high-ISP–low-PGS combination produced a mean predicted probability of 0.998 for TRF + TRU + TWS. Taken together, types containing an urban-waterlogging component were consistently associated with higher impervious-surface coverage and lower green-space coverage, whereas the differentiation of TRF + TWS from TRF involved a broader combination of topographic wetness, imperviousness and other environmental characteristics.

4. Discussion

4.1. Implications for typhoon disaster-chain management

Fujian exhibited a dual spatial pattern of typhoon disaster-chain sensitivity. TRL sensitivity was widespread across the mountainous interior, whereas TRU, TRF, and TWS sensitivity was more spatially restricted but concentrated in coastal urban districts, downstream river valleys, and low-lying estuarine areas. TRL covered the largest high-sensitivity area, while TRU covered the smallest area but showed strong local concentration in highly urbanized districts. Spatial extent and local concentration therefore represent distinct dimensions of disaster-chain sensitivity and should be considered separately in

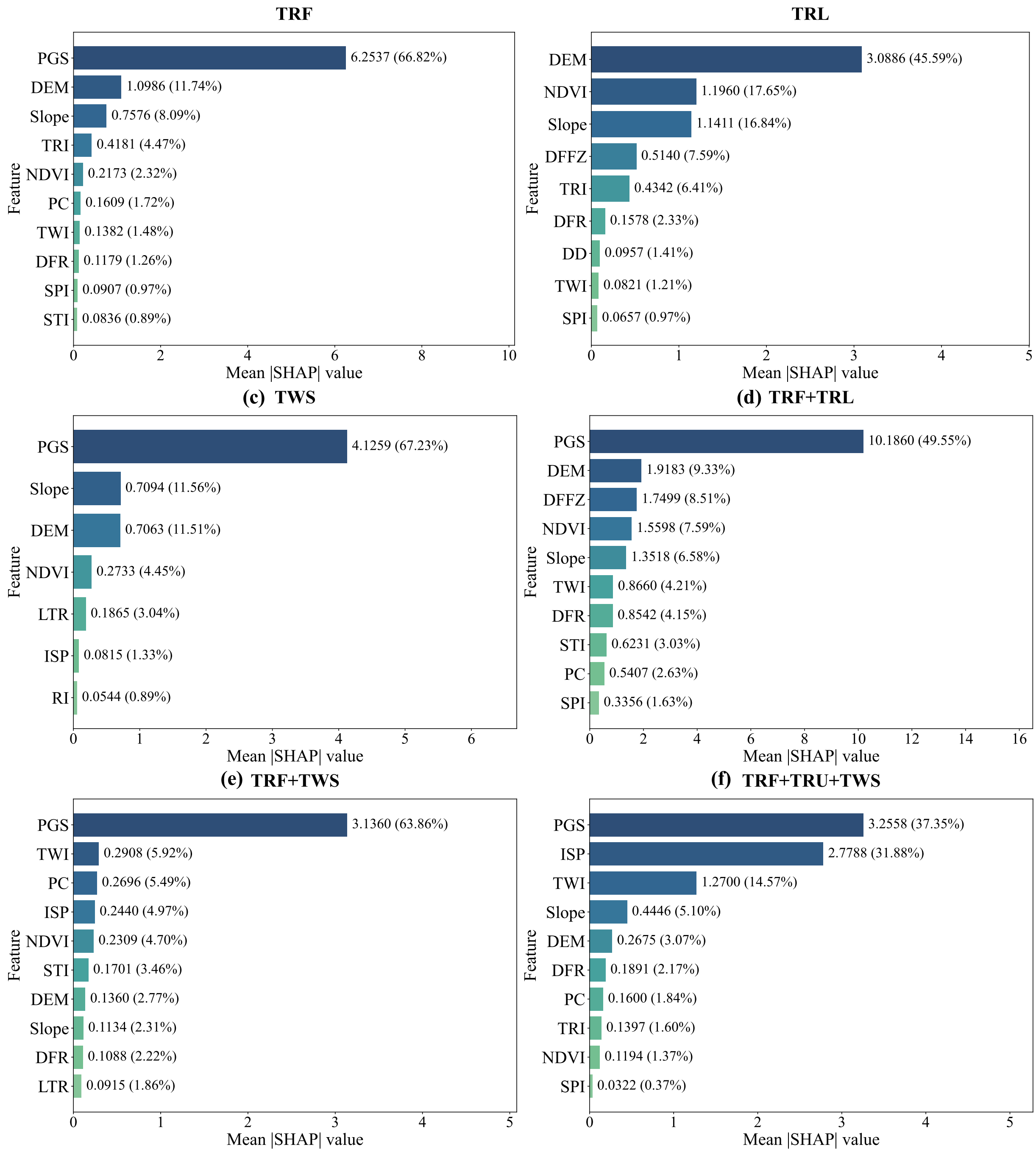

Fig. 7. Environmental contributions to the differentiation of mapped disaster-chain types. Bars show the mean absolute SHAP values derived from spatially validated XGBoost models. Values beside the bars indicate the mean absolute SHAP value and its percentage contribution relative to all predictors included in the corresponding model. Only the ten highest-ranked predictors are shown for models containing more than ten variables.

regional management. Similar coastal–inland contrasts have been reported in studies of typhoon-related and multi-hazard risks in coastal regions (Ganguli and Lin, 2025; Moreno et al., 2024; Lockwood et al., 2024).

Compound disaster-chain types occupied a limited proportion of the total high-sensitivity area but were concentrated in specific coastal and urban settings. TRF + TWS accounted for most of the compound-type area, followed by TRF + TRU + TWS and TRF + TRU. No TRU-only type was identified, indicating that high TRU sensitivity generally co-occurred spatially with high TRF sensitivity. The limited area of compound types should therefore not be interpreted as limited management relevance, because these types occurred where environmental conditions associated with river flooding, urban waterlogging, and storm surge overlapped. This result supports previous findings that interacting hazards may not be adequately represented by separate single-hazard assessments (Gill and Malamud, 2014; Zscheischler et al., 2018; Jäger et al., 2025).

Environmental differentiation among disaster-chain types was type-specific rather than governed by a common set of thresholds. Green-space coverage was the leading variable for most flood- and coastal-related types, whereas elevation was the leading variable for TRL. Pairwise models further showed that types containing a TRU component were generally associated with higher impervious-surface coverage and lower green-space coverage. In contrast, the differentiation of TRF +

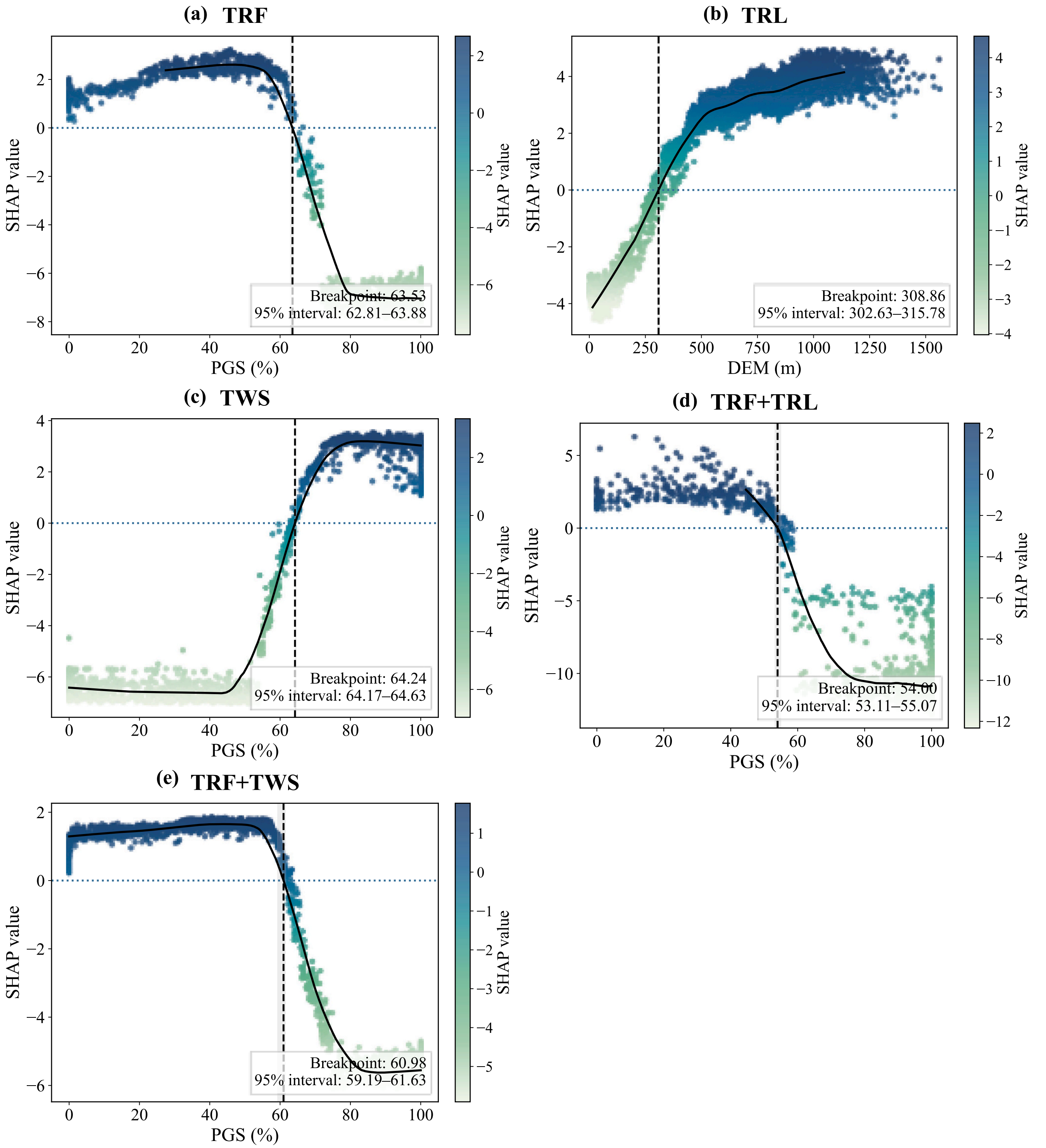

Fig. 8. Nonlinear associations between leading environmental variables and mapped disaster-chain types. Points show SHAP values, black curves show LOWESS-smoothed relationships, and horizontal dotted lines indicate SHAP = 0. Vertical dashed lines mark the principal SHAP zero crossings, with shaded regions showing their 95% spatial block-bootstrap intervals.

TWS from TRF involved topographic wetness, imperviousness, and other environmental variables. The identified SHAP differentiation points mark changes in the sign of predictor contributions within the observed environmental range and do not represent physical thresholds for disaster occurrence.

4.2. Recommendations for prevention and mitigation

The contrasting spatial pattern supports differentiated management for coastal urban areas and inland mountainous areas. In highly urbanized districts such as Taijiang and Huli, measures should focus on reducing sensitivity associated with TRU and its compound types. Areas with high impervious-surface coverage and limited green space should receive priority for drainage improvement and blue–green

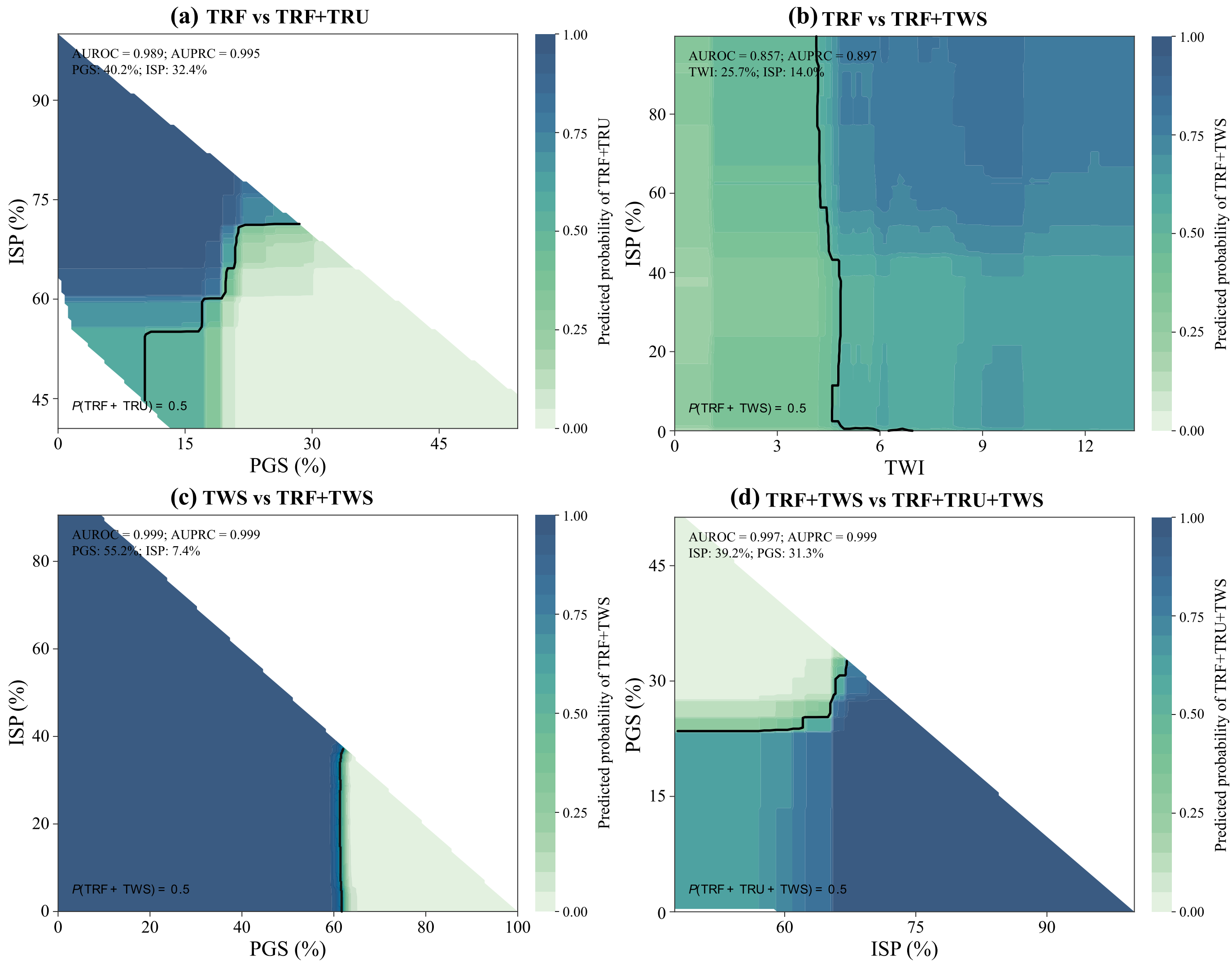

Fig. 9. Pairwise environmental differentiation of selected disaster-chain types. Colours show the predicted probability of TRF + TRU in (a), TRF + TWS in (b, c), and TRF + TRU + TWS in (d), with all other predictors fixed at their pair-specific median values. Black contours mark $P = 0.5$, and white regions lie outside the observed bivariate support. Values in each panel report spatial holdout performance and the relative SHAP contributions of the two displayed predictors.

infrastructure, including permeable surfaces, rain gardens, retention areas, urban green spaces, and restored waterways (Venkataramanan et al., 2019; Zhang et al., 2024). These measures should be integrated with land-use control and drainage-system upgrading rather than implemented independently (Qin et al., 2025; Yang et al., 2026).

Management of TRF + TWS sensitivity should consider the combined influence of downstream river conditions, coastal water levels, and local drainage constraints. Monitoring of upstream discharge and coastal water levels should be coordinated, particularly in low-lying estuarine areas. Relevant measures may include improved drainage outlets, protection of low-lying infrastructure, and emergency plans that account for possible river-coast interactions. Because the present results represent environmental sensitivity rather than event-specific hazard probabilities, local hydrological and engineering assessments remain necessary.

In inland mountainous areas, prevention should focus on TRL sensitivity, particularly in Nanping and Sanming. Priority measures include slope monitoring, rainfall-based landslide warning, vegetation restoration, slope drainage, and reinforcement of unstable slopes where necessary (Liu et al., 2022; Lin et al., 2024; Grimley et al., 2024). The elevation-related SHAP differentiation point can serve as a regional screening reference but does not represent a universal threshold for slope instability.

The scale dependence of disaster-chain types also has practical implications. Differences between predominant empirical types and model-supported types decreased from the county scale to the basin scale, while TRL became increasingly dominant at broader scales. This indicates that city- and basin-level aggregation can obscure localized compound-type heterogeneity. Units with high empirical type entropy require more flexible preparedness because several disaster-chain types may occupy substantial proportions of the same unit. Regional planning should therefore combine basin-scale coordination with county- and district-level hotspot identification. Digital twins, remote sensing, and multi-hazard early-warning systems may support scenario analysis and coordinated response in these areas (Ghaffarian, 2025; Zamanian et al., 2025; Tiggeloven et al., 2026).

4.3. Result validation and method transferability

Direct validation of disaster-chain sensitivity is difficult because historical disaster records are commonly reported by event or administrative unit and are rarely classified by specific disaster-chain type. Grid-scale validation using observed chain-specific impacts was therefore not feasible. Similar limitations have been reported in multi-hazard and compound-impact studies, where records often lack information on hazard interactions and process sequences (Chen et al., 2026; Jäger et al., 2025; Tiggeloven et al., 2026). We therefore assessed the geographical, statistical, and physical consistency of the results. These assessments provide consistency checks rather than independent observational validation.

The mapped spatial pattern was broadly consistent with the physical environment of Fujian. High TRU, TRF, and TWS sensitivity was concentrated in coastal urban districts, downstream river valleys, and low-lying estuarine areas, whereas high TRL sensitivity occurred mainly in mountainous and hilly areas (Li et al., 2022; Liu et al., 2022; Lin et al., 2024). The dependence structure was also geographically interpretable. TRF and TRU showed strong positive dependence in urban areas, and TRF and TWS showed moderate positive dependence within the coastal zone. By contrast, the negative dependence of TRL with TRF and TWS reflected their contrasting mountainous and coastal settings. These relationships indicate that the fitted dependence structure was consistent with the spatial organization of the underlying DFE sensitivity indices. Copula-based methods have also been used to characterize dependence between hydrological and coastal processes (Couasnon et al., 2018; Deb et al., 2024).

The close agreement between area-weighted Copula probabilities and empirical spatial proportions provided an additional internal consistency check. SHAP results also produced environmentally interpretable differentiation among the mapped types. However, SHAP values represent predictor contributions to model classification and should not be interpreted as direct causal effects (Lundberg and Lee, 2017; Rudin, 2019). Model performance also differed among types. The TRF + TRU one-versus-rest model showed weaker discrimination and was excluded from the main SHAP interpretation. Conclusions for this type were therefore based mainly on the better-performing pairwise model.

The framework is transferable to other typhoon-prone coastal regions, but local adaptation is required. Its main components—DFE sensitivity assessment, spatially conditioned dependence modelling, disaster-chain type delineation, multiscale comparison, and spatially validated XGBoost–SHAP analysis—can be applied elsewhere. However, the indicator system, high-sensitivity classification criteria, applicability domains, and disaster-chain types should be recalibrated, whereas the SHAP-derived differentiation points should be re-estimated according to local climate, terrain, drainage, coastal morphology, land use, and data availability. The workflow is therefore transferable, whereas the mapped types and environmental relationships remain region-specific.

4.4. Limitations and future research

Despite its contributions, this study has several limitations. The mapped disaster-chain types represent spatial patterns of DFE sensitivity rather than observed hazard sequences, event probabilities, or disaster losses. The assessment was mainly based on reanalysis and geospatial datasets. Although these data support consistent provincial-scale analysis, they may not fully capture microtopographic effects, local drainage capacity, short-duration extremes, or local engineering conditions. Some processes, particularly urban inundation and storm surge, were represented indirectly because consistent high-resolution observations remain limited. In addition, differences in indicator composition among disaster chains may affect the environmental information represented by each sensitivity index and introduce uncertainty into cross-chain comparisons. Spatial aggregation at the city and basin scales may also reduce localized compound-type heterogeneity. This study focused on environmental sensitivity rather than a comprehensive hazard–exposure–vulnerability risk assessment, and direct grid-scale validation was constrained by the lack of chain-specific observations and loss records.

Further research should strengthen independent validation using event-based inundation maps, tide-gauge observations, landslide inventories, rainfall records, and local drainage data. The robustness of the framework should also be assessed using alternative and common indicator sets, different classification criteria, and independent event cases. Integrating DFE sensitivity with hazard intensity, socio-economic exposure, vulnerability, emergency capacity, and observed losses would support a more comprehensive risk assessment, while extending the framework to climate- and land-use-change scenarios would help evaluate possible changes in typhoon disaster-chain sensitivity.

5. Conclusion

This study developed a multiscale framework for characterizing the spatial patterns, dependence structures, multiscale organization, and environmental differentiation of single and compound typhoon disaster-chain sensitivity in Fujian Province. The main conclusions are as follows.

(1) Typhoon disaster-chain sensitivity exhibited a dual spatial pattern, with widespread landslide-related sensitivity in the mountainous interior and localized flood-, waterlogging-, and storm-surge-related sensitivity in coastal areas. High-sensitivity areas for typhoon-rainstorm-urban waterlogging (TRU), typhoon-rainstorm-flooding (TRF), typhoon-rainstorm-landslide (TRL), and typhoon-wind-storm surge (TWS) accounted for 0.7%, 5.6%, 31.6%, and 5.0% of Fujian, respectively. TRL sensitivity was widely distributed across inland mountainous and hilly areas, whereas high-sensitivity areas for TRU, TRF, and TWS were concentrated in coastal urban districts, downstream river valleys, and low-lying estuarine areas. Although TRU had the smallest high-sensitivity area, it was strongly concentrated in highly urbanized districts, accounting for 91.7% and 87.4% of the areas of Taijiang and Huli, respectively.

(2) The four disaster chains exhibited distinct dependence structures and spatial combinations. TRF and TRU showed the strongest positive dependence in urban areas (Kendall's $\tau = 0.834$), and no TRU-only type was identified, indicating that areas of high TRU sensitivity generally coincided spatially with areas of high TRF sensitivity. Areas highly sensitive to at least one disaster chain covered 42.0% of Fujian. Within this area, single-chain and compound types accounted for 93.1% and 6.9%, respectively. TRF + TWS was the predominant compound type, representing 69.4% of the compound-type area.

(3) The spatial organization of disaster-chain types was scale-dependent. TRL was the predominant empirical type in 71.8% of counties, 88.9% of cities, and all basins. The mismatch between predominant empirical types and model-supported types decreased from 12.9% at the county scale to 11.1% at the city scale and disappeared at the basin scale. These findings indicate that broader-scale aggregation increases the apparent dominance of TRL while potentially obscuring localized compound-type heterogeneity, underscoring the importance of multiscale analysis in disaster-chain sensitivity assessment and regional management.

(4) Environmental associations differed among disaster-chain types. Green-space proportion was the leading environmental discriminator for most flood- and coastal-related types, accounting for 37.4–67.2% of the total mean absolute SHAP value, whereas elevation was the leading discriminator for TRL, with a contribution of 45.6%. Compound types containing a TRU component were generally associated with higher impervious-surface coverage and lower green-space coverage.

Overall, this study provides an integrated multiscale framework for assessing single and compound typhoon disaster-chain sensitivity. The findings can support hotspot identification and type-specific disaster-chain management in typhoon-prone coastal regions. The framework can be adapted to other regions, but the indicator system, high-sensitivity classification criteria, spatial applicability domains, and locally relevant disaster-chain types should be recalibrated, whereas model-derived differentiation points should be re-estimated according to local environmental conditions and data availability.

CRediT authorship contribution statement

Xiaoliu Yang: Writing – original draft, Data curation, Methodology, Software, Formal analysis. **Laiyin Zhu:** Methodology, Writing – review & editing. **Xiaochen Qin:** Data curation, Software. **Xiang Zhou:** Methodology. **Miaomiao Ma:** Data curation, Software. **Jiewen You:** Methodology. **Ying Chen:** Methodology. **Jianhui Wei:** Methodology. **Lu Gao:** Supervision, Investigation, Resources, Conceptualization, Writing – review & editing. **Harald Kunstmann:** Methodology.

Declaration of competing interest

The authors declare that they have no known competing financial interests or personal relationships that could have appeared to influence the work reported in this paper.

Acknowledgements

This work was funded by the National Natural Science Foundation of China (Grant No. 42271030), the "Young Eagle Plan" Top Talents of Fujian Province, the Key Project of the Natural Science Foundation of Fujian Province (Grant No. 2026J002025), and the Federal Ministry of Education and Research (BMBF) through the KARE II project (Grant No. 01LR2006D1). Jianhui Wei was supported by the KARE II project (Grant No. 01LR2006D1). Lu Gao was supported by the Humboldt Research Fellowship for Experienced Researchers from the Alexander von Humboldt Foundation.

Appendix A. Supplementary data

Supplementary data to this article can be found online at https://doi.org/10.1016/j.cliser.2026.100706.

Data availability

Data will be made available on request.

References

Aas, K., Czado, C., Frigessi, A., Bakken, H., 2009. Pair-copula constructions of multiple dependence. Insur. Math. Econ. 44, 182–198. https://doi.org/10.1016/j.insmatheco.2007.02.001.

Bhardwaj, P., Singh, O., Yadav, R.B.S., 2020. Probabilistic assessment of tropical cyclones' extreme wind speed in the Bay of Bengal: implications for future cyclonic hazard. Nat. Hazards 101, 275–295. https://doi.org/10.1007/s11069-020-03873-5.

Bi, S., Chen, M., Dai, F., 2022. The impact of urban green space morphology on PM2.5 pollution in Wuhan, China: a novel multiscale spatiotemporal analytical framework. Build. Environ. 221, 109340. https://doi.org/10.1016/j.buildenv.2022.109340.

Bodoque, J., Esteban-Muñoz, Á., Ballesteros-Cánovas, J., 2023. Overlooking probabilistic mapping renders urban flood risk management inequitable. Commun. Earth Environ. 4, 279. https://doi.org/10.1038/s43247-023-00940-0.

Cai, J., Yang, J., Liu, M., Fang, W., Ma, Z., Bi, J., 2024. Informing urban flood risk adaptation by integrating human mobility big data during heavy precipitation. Environ. Sci. Technol. 58, 4617–4626. https://doi.org/10.1021/acs.est.3c03145.

Chen, A., Pokhrel, Y., Chen, D., Huang, H., Dai, Z., He, B., Wang, J., Li, J., Wang, H., Liu, J., 2024. Impact of tropical cyclones and socioeconomic exposure on flood risk distribution in the Mekong Basin. Commun. Earth Environ. 5, 704. https://doi.org/10.1038/s43247-024-01868-9.

Chen, W., Zheng, Y., Zhou, Y., Zhou, Y., Zhang, T., Zhang, Y., Zhu, A., Zhou, X., Zhang, X., Huang, D., 2026. Global acceleration of compound flood risks through fluvial-tidal interactions in a warming climate. npj Nat. Hazards 3, 13. https://doi.org/10.1038/s44304-026-00179-7.

Couasnon, A., Sebastian, A., Morales-Nápoles, O., 2018. A copula-based Bayesian network for modeling compound flood hazard from riverine and coastal interactions at the catchment scale: An application to the Houston Ship Channel, Texas. Water 10, 1190. https://doi.org/10.3390/w10091190.

Dawit, G.B., Shankar, K., Gemachu, S., 2023. Identifying flood vulnerable and risk areas using the integration of analytical hierarchy process, GIS, and remote sensing: a case study of southern Oromia region. Urban Clim. 51, 101640. https://doi.org/10.1016/j.uclim.2023.101640.

Deb, M., Sun, N., Yang, Z., Wang, T., Judi, D.R., Xiao, Z., Wigmosta, M.S., 2023. Interacting effects of watershed and coastal processes on the evolution of compound flooding during Hurricane Irene. Earth's Future 11, e2022EF002947. https://doi.org/10.1029/2022EF002947.

Deb, M., Benedict, J., Sun, N., Yang, Z., Robert, H., David, J., Wang, T., 2024. Estuarine hurricane wind can intensify surge-dominated extreme water level in shallow and converging coastal systems. Nat. Hazards Earth Syst. Sci. 24, 2461–2479. https://doi.org/10.5194/nhess-24-2461-2024.

Dey, H., Haque, M.M., Shao, W., VanDyke, M., Hao, F., 2024. Simulating flood risk in Tampa Bay using a machine learning driven approach. npj Nat. Hazards 1, 40. https://doi.org/10.1038/s44304-024-00045-4.

Dolojan, N., Takahashi, T., Hashimoto, M., Shibayama, A., Nomura, R., Terada, K., Moriguchi, S., 2025. Integrated multihazard study combining qualitative and quantitative analyses of floods, landslides, and debris flows: a case study on the impacts of Typhoon Yun Yeung on Iwaki City, Fukushima. Int. J. Disaster Risk Reduct. 127, 105647. https://doi.org/10.1016/j.ijdrr.2025.105647.

Dou, J., Yunus, A.P., Merghadi, A., Shirzadi, A., Nguyen, H., Hussain, Y., Avtar, R., Chen, Y., Pham, B.T., Yamagishi, H., 2020. Different sampling strategies for predicting landslide susceptibilities are deemed less consequential with deep learning. Sci. Total Environ. 720, 137320. https://doi.org/10.1016/j.scitotenv.2020.137320.

Dullaart, J., Muis, S., Bloemendaal, N., Chertova, M., Couasnon, A., Aerts, J., 2021. Accounting for tropical cyclones more than doubles the global population exposed to low-probability coastal flooding. Commun. Earth Environ. 2, 135. https://doi.org/10.1038/s43247-021-00204-9.

Ermagun, A., Smith, V., Janatabadi, F., 2024. High urban flood risk and no shelter access disproportionally impacts vulnerable communities in the USA. Commun. Earth Environ. 5, 2. https://doi.org/10.1038/s43247-023-01165-x.

Falguni, M., Singh, D., 2020. Detecting flood prone areas in Harris county: a GIS based analysis. GeoJournal 85, 647–663. https://doi.org/10.1007/s10708-019-09984-2.

Ganguli, P., Lin, N., 2025. Intense humid heat-tropical cyclone compound hazards in eastern coastal India. npj Nat. Hazards 2, 49. https://doi.org/10.1038/s44304-025-00103-5.

Ganguli, P., Merz, B., 2024. Observational evidence reveals compound humid heat stress-extreme rainfall hotspots in India. Earth's Future 12, e2023EF004074. https://doi.org/10.1029/2023EF004074.

Ghaffarian, S., 2025. Rethinking digital twin: introducing digital risk twin for disaster risk management. npj Nat. Hazards 2, 79. https://doi.org/10.1038/s44304-025-00135-x.

Gill, J.C., Malamud, B.D., 2014. Reviewing and visualizing the interactions of natural hazards. Rev. Geophys. 52, 680–722. https://doi.org/10.1002/2013RG000445.

Gori, A., Lin, N., Xi, D., 2020. Tropical cyclone compound flood hazard assessment: from investigating drivers to quantifying extreme water levels. Earth's Future 8, e2020EF001660. https://doi.org/10.1029/2020EF001660.

Grimley, L.E., Hollinger Beatty, K.E., Sebastian, A., Bunya, S., Lackmann, G.M., 2024. Climate change exacerbates compound flooding from recent tropical cyclones. npj Nat. Hazards 1, 45. https://doi.org/10.1038/s44304-024-00046-3.

He, Q., Shahabi, H., Shirzadi, A., Li, S., Chen, W., Wang, N., Chai, H., Bian, H., Ma, J., Chen, Y., Wang, X., Chapi, K., Ahmad, B.B., 2019. Landslide spatial modelling using novel bivariate statistical based Naïve Bayes, RBF classifier, and RBF network machine learning algorithms. Sci. Total Environ. 663, 1–15. https://doi.org/10.1016/j.scitotenv.2019.01.329.

Hosseini, S., Ivanov, D., 2020. Bayesian networks for supply chain risk, resilience and ripple effect analysis: a literature review. Expert Syst. Appl. 161, 113649. https://doi.org/10.1016/j.eswa.2020.113649.

Intergovernmental Panel on Climate Change, 2023. Climate Change 2021: The Physical Science Basis. Working Group I Contribution to the Sixth Assessment Report of the Intergovernmental Panel on Climate Change, 1st ed. Cambridge University Press. https://doi.org/10.1017/9781009157896.

Jäger, W.S., de Ruiter, M.C., Tiggeloven, T., Ward, P.J., 2025. What can we learn about multi-hazard impacts from global disaster records? Nat. Hazards Earth Syst. Sci. 25, 2751–2769. https://doi.org/10.5194/nhess-25-2751-2025.

Kappes, M.S., Keiler, M., von Elverfeldt, K., Glade, T., 2012. Challenges of analyzing multi-hazard risk: a review. Nat. Hazards 64, 1925–1958. https://doi.org/10.1007/s11069-012-0294-2.

Karim, I., Sameh, A., Aly, E., Saber, M., Sumi, T., Almamari, M., Elboshy, B., Ghoniem, S., 2023. An integrated indicator-based approach for constructing an urban flood vulnerability index as an urban decision-making tool using the PCA and AHP techniques: a case study of Alexandria, Egypt. Urban Clim. 48, 101426. https://doi.org/10.1016/j.uclim.2023.101426.

Lee, S., Kim, J.C., Jung, H.S., Lee, M.J., Lee, S., 2017. Spatial prediction of flood susceptibility using random-forest and boosted-tree models in Seoul metropolitan city, Korea. Geomat. Nat. Hazards Risk 8, 1185–1203. https://doi.org/10.1080/19475705.2017.1308971.

Li, Z., 2022. Extracting spatial effects from machine learning model using local interpretation method: an example of SHAP and XGBoost. Comput. Environ. Urban. Syst. 96, 101845. https://doi.org/10.1016/j.compenvurbsys.2022.101845.

Li, C., Liu, M., Hu, Y., Wang, H., Zhou, R., Wu, W., Wang, Y., 2022. Spatial distribution patterns and potential exposure risks of urban floods in Chinese megacities. J. Hydrol. 610, 127838. https://doi.org/10.1016/j.jhydrol.2022.127838.

Li, Y., Zhou, W., Shen, P., 2023. Flood risk assessment of loss of life for a coastal city under the compound effect of storm surge and rainfall. Urban Clim. 47, 101396. https://doi.org/10.1016/j.uclim.2022.101396.

Lin, J., He, P., Yang, L., He, X., Lu, S., Liu, D., 2022. Predicting future urban waterlogging-prone areas by coupling the maximum entropy and FLUS model. Sustain. Cities Soc. 80, 103812. https://doi.org/10.1016/j.scs.2022.103812.

Lin, M., Chen, G., Hu, B., Bassir, D., 2024. Stability factor prediction of multilayer slope using three-dimensional convolutional neural network based on digital twin and prior knowledge data. Environ. Earth Sci. 83, 259. https://doi.org/10.1007/s12665-024-11562-w.

Liu, A., Wu, H., Liang, G., Cardenas-Tristan, A., Wu, X., Zhao, C., Li, D., 2020. A big data-driven dynamic estimation model of relief supplies demand in urban flood disaster. Int. J. Disaster Risk Reduct. 49, 101682. https://doi.org/10.1016/j.ijdrr.2020.101682.
Liu, X., Wang, Y., Koo, R.C.H., Kwan, J.S.H., 2022. Development of a slope digital twin for predicting temporal variation of rainfall-induced slope instability using past slope performance records and monitoring data. Eng. Geol. 308, 106825. https://doi.org/10.1016/j.enggeo.2022.106825.
Liu, X., Liu, Y., Wang, Z., Yang, X., Zeng, X., Meng, D., 2023. Comprehensive assessment of vulnerability to storm surges in coastal China: towards a prefecture-level cities perspective. Remote Sens. 15, 4828. https://doi.org/10.3390/rs15194828.
Lockwood, J.W., Lin, N., Gori, A., Oppenheimer, M., 2024. Increasing flood hazard posed by tropical cyclone rapid intensification in a changing climate. Geophys. Res. Lett. 51, e2023GL105624. https://doi.org/10.1029/2023GL105624.
Lundberg, S.M., Lee, S.-I., 2017. A unified approach to interpreting model predictions. Adv. Neural Inf. Proces. Syst. 30, 4765–4774. https://doi.org/10.5555/3295222.3295230.
Ma, T., Yu, W., Speich, S., Zhao, H., Xin, R., Luo, H., Wu, L., 2025. Philippine archipelago and South China Sea monsoon plus ocean cooling buffer Northwestern Pacific super typhoons. Nat. Commun. 16, 7395. https://doi.org/10.1038/s41467-025-62334-4.
Meng, D., Liu, Y., Wang, Z., Yang, X., Liu, X., Zhang, J., Gao, K., 2023. Decreasing vulnerability of storm surge disasters in coastal cities of China over the past 30 years. J. Mar. Sci. Eng. 11, 128. https://doi.org/10.3390/jmse11010128.
Moore, I.D., Grayson, R.B., Ladson, A.R., 1991. Digital terrain modelling: a review of hydrological, geomorphological, and biological applications. Hydrol. Process. 5, 3–30. https://doi.org/10.1002/hyp.3360050103.
Moreira, L., de Brito, M., Kobiyama, M., 2021. Review article: a systematic review and future prospects of flood vulnerability indices. Nat. Hazards Earth Syst. Sci. 21, 1513–1530. https://doi.org/10.5194/nhess-21-1513-2021.
Moreno, M., Lombardo, L., Crespi, A., Zellner, P., Mair, V., Pittore, M., Westen, C., Steger, S., 2024. Space-time data-driven modeling of precipitation-induced shallow landslides in South Tyrol, Italy. Sci. Total Environ. 912, 169166. https://doi.org/10.1016/j.scitotenv.2023.169166.
Peng, Z., Mo, S., Sun, A., Wu, J., Zeng, X., Lu, M., Shi, X., 2025. An explainable Bayesian TimesNet for probabilistic groundwater level prediction. Water Resour. Res. 61, e2025WR040191. https://doi.org/10.1029/2025WR040191.
Qin, X., Wu, Y., Huang, H., Yang, X., Gao, L., 2025. Impact of impervious surface spatial morphologies on urban waterlogging: insights from a cascade modeling chain at catchment scale. Sustain. Cities Soc. 15, 106912. https://doi.org/10.1016/j.scs.2025.106912.
Riley, S.J., DeGloria, S.D., Elliot, R., 1999. A terrain ruggedness index that quantifies topographic heterogeneity. Intermountain J. Sci. 5, 23–27.
Rudin, C., 2019. Stop explaining black box machine learning models for high stakes decisions and use interpretable models instead. Nat. Mach. Intell. 1, 206–215. https://doi.org/10.1038/s42256-019-0048-x.
Sakahira, F., Hiroi, U., 2021. Designing cascading disaster networks by means of natural language processing. Int. J. Disaster Risk Reduct. 66, 102623. https://doi.org/10.1016/j.ijdrr.2021.102623.
Salman, A., Hazhir, A., Kamran, C., Afshar, R.S., Ebrahimi, B., 2023. Fuzzy flash flood risk and vulnerability assessment for the city of Sanandaj, Kurdistan Province, Iran. Nat. Hazards 115, 237–259. https://doi.org/10.1007/s11069-022-05552-z.
Schwarz, I., Kuleshov, Y., 2022. Flood vulnerability assessment and mapping: a case study for Australia's Hawkesbury-Nepean Catchment. Remote Sens. 14, 4894. https://doi.org/10.3390/rs14194894.
Shi, P., Ye, T., Wang, Y., Zhou, T., Xu, W., Du, J., Wang, J., Li, N., Huang, C., Liu, L., Chen, B., Su, Y., Fang, W., Wang, M., Hu, X., Wu, J., He, C., Zhang, Q., Ye, Q., Jaeger, C., Okada, N., 2020. Disaster risk science: a geographical perspective and a research framework. Int. J. Disaster Risk Sci. 11, 426–440. https://doi.org/10.1007/s13753-020-00296-5.
Sohrabi, M., Moftakhari, H., Moradkhani, H., 2023. Efficient tropical cyclone scenario selection based on cumulative likelihood of potential impacts. Earth's Future 11, e2023EF003731. https://doi.org/10.1029/2023EF003731.
Tang, P., Zhong, W., Wen, J., Zhou, D.P., Huang, S.Q., 2023. Developing and understanding cascading effects scenario of typhoons in coastal mega-cities from system perspectives for disaster risk reduction: a case study of Shenzhen, China. Int. J. Disaster Risk Reduct. 92, 103691. https://doi.org/10.1016/j.ijdrr.2023.103691.
Tiggeloven, T., Raymond, C., de Ruiter, M.C., Sillmann, J., Thieken, A.H., Buijs, S.L., Ciurean, R., Cordier, E., Crummy, J.M., Cumiskey, L., De Polt, K., Duncan, M., Ferrario, D.M., Jäger, W.S., Koks, E.E., van Maanen, N., Murdock, H.J., Mysiak, J., Nirandjan, S., Poschlod, B., Priesmeier, P., Sairam, N., Schweizer, P.-J., Stolte, T.R., Zenker, M.-L., Daniell, J.E., Fekete, A., Geiß, C.M., van den Homberg, M.J.C., Juhola, S.K., Kuhlicke, C., Lebek, K., Šakić Trogrlić, R., Schneiderbauer, S., Torresan, S., van Westen, C.J., Claassen, J.N., Khazai, B., Murray, V., Schlumberger, J., Ward, P.J., 2026. Multi-hazard risk assessment and management: pathways for the Sendai framework and beyond. Geosci. Commun. 9, 185–221. https://doi.org/10.5194/gc-9-185-2026.
Venkataramanan, V., Packman, A.I., Peters, D.R., Lopez, D., McCuskey, D.J., McDonald, R.I., Miller, W.M., Young, S.L., 2019. A systematic review of the human health and social well-being outcomes of green infrastructure for stormwater and flood management. J. Environ. Manag. 246, 868–880. https://doi.org/10.1016/j.jenvman.2019.05.028.
Wang, Y., Song, C., Lin, Q.G., Li, J., 2016. Occurrence probability assessment of earthquake-triggered landslides with Newmark displacement values and logistic regression: the Wenchuan earthquake, China. Geomorphology 258, 108–119. https://doi.org/10.1016/j.geomorph.2016.01.004.
Wang, N., Zhang, H., Ashok, D., Cheng, W., Zhao, M., Lombardo, L., 2024. On the use of explainable AI for sensitivity modeling: examining the spatial pattern of SHAP values. Geosci. Front. 15, 101800. https://doi.org/10.1016/j.gsf.2024.101800.
Wu, M., Wu, Z., Ge, W., Wang, H., Shen, Y., Jiang, M., 2021. Identification of sensitivity indicators of urban rainstorm flood disasters: a case study in China. J. Hydrol. 599, 126393. https://doi.org/10.1016/j.jhydrol.2021.126393.
Xi, D., Lin, N., Gori, A., 2023. Increasing sequential tropical cyclone hazards along the US East and Gulf coasts. Nat. Clim. Chang. 13, 258–265. https://doi.org/10.1038/s41558-023-01595-7.
Xiao, S., Zou, L., Xia, J., Dong, Y., Yang, Z.Z., Yao, T.C., 2023. Assessment of the urban waterlogging resilience and identification of its driving factors: a case study of Wuhan City, China. Sci. Total Environ. 866, 161321. https://doi.org/10.1016/j.scitotenv.2022.161321.
Yang, X., Qin, X., Zhou, X., Chen, Y., Gao, L., 2024. Assessment of disaster mitigation capability oriented to typhoon disaster chains: a case study of Fujian Province, China. Ecol. Indic. 167, 112621. https://doi.org/10.1016/j.ecolind.2024.112621.
Yang, X., Yan, Y., Zhou, L., Ma, M., Zhang, J., Chen, Y., Gao, L., 2025. Risk of compound typhoon disaster chains: insights from Southeastern China. Int. J. Disaster Risk Sci. 16, 870–887. https://doi.org/10.1007/s13753-025-00674-x.
Yang, X., Qin, X., Ma, M., You, J., Chen, Y., Zhu, L., Wei, J., Gao, L., 2026. A Copula-XAI framework for assessing compound typhoon disaster-chain risks and driving mechanisms in coastal mountainous cities: evidence from Fujian, China. J. Hydrol. Reg. Stud. 64, 103284. https://doi.org/10.1016/j.ejrh.2026.103284.
Ye, P., Yu, B., Chen, W.H., Liu, K., Ye, L., 2022. Rainfall induced landslide sensitivity mapping using machine learning algorithms and comparison of their performance in Hilly area of Fujian Province, China. Nat. Hazards 113, 965–995. https://doi.org/10.1007/s11069-022-05332-9.
Yu, C., David, A., 2022. Integrated flood risk assessment of river basins: application in the Dadu river basin, China. J. Hydrol. 613, 128456. https://doi.org/10.1016/j.jhydrol.2022.128456.
Zamanian, M., Payan, M., Salimi, M., Qahremani, F., Arabani, M., Shalchian, M.M., 2025. Comparative efficacy of grouting and mixing methods for stabilizing collapsible soils with nano-clay and cement. Case Stud. Constr. Mater. 8, e05159. https://doi.org/10.1016/j.cscm.2025.e05159.
Zeng, Z., Lai, C., Wang, Z., Chen, Y., Chen, X., 2024. Future sea level rise exacerbates compound floods induced by rainstorm and storm tide during super typhoon events: a case study from Zhuhai, China. Sci. Total Environ. 911, 168799. https://doi.org/10.1016/j.scitotenv.2023.168799.
Zhang, Q., Wu, Z., Guo, G., Zhang, H., Tarolli, P., 2021. Explicit the urban waterlogging spatial variation and its driving factors: the stepwise cluster analysis model and hierarchical partitioning analysis approach. Sci. Total Environ. 763, 143041. https://doi.org/10.1016/j.scitotenv.2020.143041.
Zhang, C., Yang, W., Jiang, X., Lian, J., Hu, D., Yan, X., Yan, L., 2024. A novel integrated urban flood risk assessment approach coupling GeoDetector-Dematel and clustering method. J. Environ. Manag. 354, 120308. https://doi.org/10.1016/j.jenvman.2024.120308.
Zhou, C., Ye, M., Xia, Z., Wang, W., Luo, C., Muller, J., 2025. An interpretable attention-based deep learning method for landslide prediction based on multi-temporal InSAR time series: a case study of Xinpu landslide in the TGRA. Remote Sens. Environ. 318, 114580. https://doi.org/10.1016/j.rse.2024.114580.
Zhuang, Y., Xing, A., Sun, Q., Jiang, Y., Zhang, Y., Wang, C., 2023. Failure and disaster causing mechanism of a typhoon induced large landslide in Yongjia, Zhejiang, China. Landslides 20, 2257–2269. https://doi.org/10.1007/s10346-023-02099-3.
Zscheischler, J., Westra, S., van den Hurk, B.J.J.M., Seneviratne, S.I., Ward, P.J., Pitman, A., Aghakouchak, A., Bresch, D.N., Leonard, M., Wahl, T., Zhang, X., 2018. Future climate risk from compound events. Nat. Clim. Chang. 8, 469–477. https://doi.org/10.1038/s41558-018-0156-3.
Zuccaro, G., De Gregorio, D., Leone, M.F., 2018. Theoretical model for cascading effects analyses. Int. J. Disaster Risk Reduct. 30, 199–215. https://doi.org/10.1016/j.ijdrr.2018.04.019.